Phase-field simulation of the microstructure evolution in lath martensitic steels

Zhenhua CONG

Nagoya University

July 2012

Content

Chapter 1 General Introduction 1

1.1 Background 1
1.1.1 Martensitic transformation and the microstructure in lath martensitic steels 1
1.1.2 Prediction of the microstructural evolution by simulation based on the phase-field method 5
1.2 Purposes of present study 7
1.3 Organization of the thesis 8
References 10

Chapter 2 Microstructure Simulation of Lath Martensite Phase by Elasto-Plastic Phase-Field Model 12

2.1 Introduction 12
2.2 Two types of slip deformation (TTSD) model 13
2.2.1 Lattice deformation 14
2.2.2 Plastic deformation 14
2.3 Elasto-plastic phase-field model 16
2.3.1 Energy description of martensitic transformation 19
2.3.2 Numerical simulation 24
2.4 Results and discussion 26
2.5 Conclusions 39
References 40

Chapter 3 Prediction of Maximum Dislocation Density in Lath Martensite by Phase-field Simulation 42

3.1 Introduction 42
3.2 Evaluation method 43
3.3 Results and discussion 47
3.4 Conclusions 49
References 50

Chapter 4 Dislocation Density of Lath Martensite in 10Cr–5W Heat-Resistant Steels 51

4.1 Introduction 51
4.2 XRD profile analysis 52
4.3 Experimental procedures 55

4.4 Results and discussion 56
4.5 Conclusions 63
References 65

Chapter 5 Morphological Observation of Lath Martensite in Fe-Cr-C Steels 67

5.1 Introduction 67
5.2 Experimental procedures 68
5.3 Results and discussion 69
5.3.1 OM observation 69
5.3.2 EBSP observation 70
5.4 Conclusions 74
References 75

Chapter 6 General Conclusions 76

Paper List Related to the Present Study 79

Acknowledgements 80

Chapter 1

General Introduction

1.1 Background

1.1.1 Martensitic transformation and the microstructure in lath martensitic steels

Martensitic transformation is still one of the most studied state reactions. The transformation has specific features that distinguish itself from the convetional phase transformations described by classical Gibbs thermodynamics. These features include (i) the occurrence of a thermoelastic two-phase equilibrium within a certain temperature range; (ii) the stress-induced transformation and related hysteresis; (iii) the shape memory effect and (iv) the appearance of a typical "martensitic" microstructure consisting of internally twinned plates or densely packed dislocations **[1-1]**. The martensite phase is formed from the austenite phase by displacive or structural phase transformation without long-range atomic diffusion, which is called martensitic tansformation. Because the martensite phase exhibits desirable mechanical properties and is used as an important constituent phase of high-strength steel, the metallurgical, crystallographical and mechanical properties of steel containing a martensitic microstructure have been intensively studied experimentally and theoretically **[1-2~1-5]**. The martensite phase is produced by the shear deformation of the crystal lattice of the parent phase. In particular, the *fcc-bcc* martensitic

transformation in a ferrous alloy is described using the Bain distortion **[1-6]**. Due to this distortion, the ratio of lattice parameters of martensite phase, i.e., c/a changes, resulting in that elastic strain is generated in the material during the martensitic transformation. Therefore, the morphology of the martensitic microstructure is characterized by the minimization path of the total free energy containing the elastic strain energy. According to **[1-7~1-10]**, it is suggested that elastic strain energy is reduced by the formation of a heterogeneous array of different orientation variants of the martensitic phase (self-accommodation) and by plastic deformation (plastic accommodation). For example, in the case of the martensitic transformation in high-carbon steels, elastic strain energy is reduced mainly by self-accommodation, and consequently, a twinned martensite is formed. On the other hand, for low-carbon steel, elastic strain energy is generally minimized by plastic accommodation, where a lot of dislocations are introduced to assist the accommodation. In this case, a lath martensite is formed and dense crystal defects are introduced into the microstructure **[1-11]**. Therefore, the microstructure of lath martensite is closely related with the dislocations appearing in martensitic transformation.

In this thesis, we focus on the study of lath martensite because of its most appearance in the recent heat-resistant commercial steels. It is reported that the lath martensite has relatively high martensite start (*M*s) tempretures and the habit plane is near $\{557\}_\gamma$ and $\{111\}_\gamma$ **[1-12]**. Moreover, the crystal orientation relationship between lath martensite and austenite is near the Kurdjumov-Sachs (K-S) relationship that is $(111)_\gamma // (011)_{\alpha'}, [\bar{1}01]_\gamma // [\bar{1}\bar{1}1]_{\alpha'}$. $(111)_\gamma$ and $(011)_{\alpha'}$ are the closed

packed planes and $\left[\bar{1}01\right]_{\gamma}$ and $\left[\bar{1}\bar{1}1\right]_{\alpha'}$ are the closed packed directions in the austenite (γ) and martensite phases (α'). There are four equivalent closed packed planes in the austenite phase, and thus there are four crystallographically different packets in an austenite grain. For the parallel direction relationships, there are three equivalent closed packed directions in the austenite phase and two equivalent closed packed directions in the martensite phase. This results in the six variants with different direction parallel relationships on the same conjugate parallel close packed plane. A total of 24 crystallographic variants in a prior austenite grain satisfy this orientation relationship is shown in Table 1-1.

Table 1-1 All 24 crystallographic variants that satisfy the K-S orientation relationship.

Variant	Plane parallel	Direction parallel	Variant	Plane parallel	Direction parallel
V1	$(111)_{\gamma}//(011)_{\alpha'}$	$[\bar{1}01]_{\gamma}//[\bar{1}\bar{1}1]_{\alpha'}$	V13	$(\bar{1}11)_{\gamma}//(011)_{\alpha'}$	$[0\bar{1}1]_{\gamma}//[\bar{1}\bar{1}1]_{\alpha'}$
V2		$[\bar{1}01]_{\gamma}//[\bar{1}1\bar{1}]_{\alpha'}$	V14		$[0\bar{1}1]_{\gamma}//[\bar{1}1\bar{1}]_{\alpha'}$
V3		$[01\bar{1}]_{\gamma}//[\bar{1}\bar{1}1]_{\alpha'}$	V15		$[\bar{1}0\bar{1}]_{\gamma}//[\bar{1}\bar{1}1]_{\alpha'}$
V4		$[01\bar{1}]_{\gamma}//[\bar{1}1\bar{1}]_{\alpha'}$	V16		$[\bar{1}0\bar{1}]_{\gamma}//[\bar{1}1\bar{1}]_{\alpha'}$
V5		$[1\bar{1}0]_{\gamma}//[\bar{1}\bar{1}1]_{\alpha'}$	V17		$[110]_{\gamma}//[\bar{1}\bar{1}1]_{\alpha'}$
V6		$[1\bar{1}0]_{\gamma}//[\bar{1}1\bar{1}]_{\alpha'}$	V18		$[110]_{\gamma}//[\bar{1}1\bar{1}]_{\alpha'}$
V7	$(1\bar{1}1)_{\gamma}//(011)_{\alpha'}$	$[10\bar{1}]_{\gamma}//[\bar{1}\bar{1}1]_{\alpha'}$	V19	$(11\bar{1})_{\gamma}//(011)_{\alpha'}$	$[\bar{1}10]_{\gamma}//[\bar{1}\bar{1}1]_{\alpha'}$
V8		$[10\bar{1}]_{\gamma}//[\bar{1}1\bar{1}]_{\alpha'}$	V20		$[\bar{1}10]_{\gamma}//[\bar{1}1\bar{1}]_{\alpha'}$
V9		$[\bar{1}\bar{1}0]_{\gamma}//[\bar{1}\bar{1}1]_{\alpha'}$	V21		$[0\bar{1}\bar{1}]_{\gamma}//[\bar{1}\bar{1}1]_{\alpha'}$
V10		$[\bar{1}\bar{1}0]_{\gamma}//[\bar{1}1\bar{1}]_{\alpha'}$	V22		$[0\bar{1}\bar{1}]_{\gamma}//[\bar{1}1\bar{1}]_{\alpha'}$
V11		$[011]_{\gamma}//[\bar{1}\bar{1}1]_{\alpha'}$	V23		$[101]_{\gamma}//[\bar{1}\bar{1}1]_{\alpha'}$
V12		$[011]_{\gamma}//[\bar{1}1\bar{1}]_{\alpha'}$	V24		$[101]_{\gamma}//[\bar{1}1\bar{1}]_{\alpha'}$

Lath martensite has a hierarchical structure consisting of packets, blocks, and laths containing densely packed complex and tangled dislocations without twins **[1-13]** as shown in Fig. 1-1. This hierarchy is as follows: (i) a prior austenite grain is composed of packets, (ii) a packet is composed of an ensemble of grains, called blocks, which have the same {111} plane as the habit plane, and (iii) a block is composed of an ensemble of single martensite crystals called laths, which have nearly the same crystal orientaion and high dislocation densities **[1-14, 1-15]**.

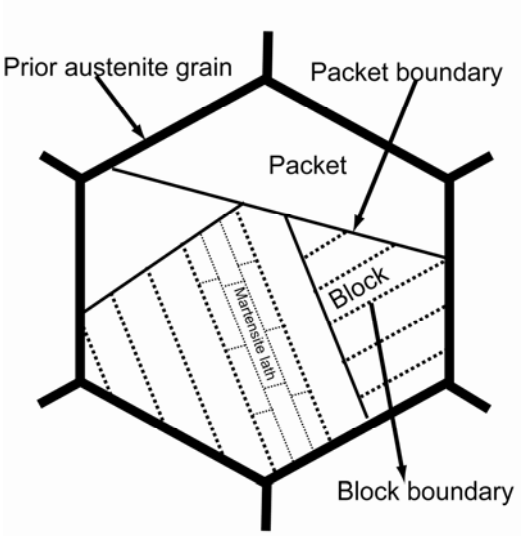

Fig.1-1 Illustration of the hierarchical lath martensite in a prior austenite grain.

Even though many researches have been dedicated to study the formation mechanism of the complex microstructure in lath martensite, it is not yet understood clearly. Recently, Iwashita et al. **[1-16]** proposed a two types of slip deformation (TTSD) model by analytical calculation to explain the formation of lath martensite. This model extends Khachaturyan's slip deformation model **[1-17]** by considering two types of plastic deformation independently to realize the martensitic transformation

without any lattice rotation. This model can exactly explain the $\{557\}_\gamma$ habit plane of lath martensite. So it is promising to reveal the microstructural information of lath martensite by the TTSD model. Change in high-temperature strength of heat-resistant steels with creep time depends on the microstructural evolution of steels at elevated temperatures. Thus, it is important to clarify the morphological evolution of lath martensite phase.

1.1.2 Prediction of the microstructural evolution by simulation based on the phase-field method

Although materials fabrication has long been known, it is only recognized in the last century that the properties of a given material might not be primarily controlled by its chemical composition but rather by its microstructures. Materials microstructures are structural features that are subject to observation under microscopy. Recently, new and more accurare techniques, such as optical microscopy (OM), transmission electron microscopy (TEM), and the electron back scattered diffraction pattern (EBSP) on scanning electron microscopy (SEM), have been developed and used to study both the microstrutures and crystallogrophy of lath martensite **[1-18]**. However, our ability to characterize and predict quantitatively microstructural evolution, which tells the unambiguous processing-property relationship, is rather limited because of both the extreme complexity of microstructure and the nonlinear interaction of its elements. By means of plausible but non-rigorous approximations, analytical approaches are suitable for only qualitative

prediction. Computational simulation is becoming an attractive alternative in developing quantitative processing-microstructure-property relationships, complementing with the traditional analytical and experimental approaches. However, it is impossible to simulate directly the huge number of atoms with an objective of predicting macroscopic properties. It remains a great challenge to simulate essential properties that depend critically upon phenomena or processes taking place at very different length and time scales. This challenge could be overcome by uncovering the elusive connections in the hierarchy of quantum/molecular, atomistic/nano, mesoscopic, and macroscopic scales. Results from simulations at the smaller length scales could feed naturally back into larger length scale models. For this sake, the simulation of the microstructure evolution at a smaller scale is sense to predict the property and formation process of materials.

Recently, a phase field method (PFM) has been extensively studied as a powerful tool for predicting microstructural evolution and has been applied to the martensitic transformation **[1-19~1-22]**. Examples of utilizing the PFM for studying microstructural evolution can be found for solidification **[1-23~1-26]**, solid-state phase transformations **[1-27]** and grain growth **[1-28]**. PFM is a field dynamic model with field variables (position and time dependent) describing arbitrary microstructures. For example, concentration field can be used to describe precipitates; long-range order parameters can be used for ordered particles; orientation field can be used for grain growth; slip field can be used for dislocations, to name but a few. The dynamics is solved in terms of total free energy reduction by dynamic equations, both having

fundamental interpretation in statistical mechanics. Depending on the physical nature of the problem, the field variables may be associated with either microscopic or mesoscopic length scale. This approach avoids the mathematically difficult problem of applying a boundary condition at an interface whose location is a part of unknown solution. It permits to solve the problem by integrating a set of partial differential equations for the whole system, and thus it is achievable to model realistic microstructures in two or three dimensions using PFM.

1.2 Purposes of present study

In the recent heat-resistant steels, which has high creep strength at elevated tempretures, the carbon content is about 0.1 mass%, where lath martensite always appears. As mentioned in 1.1.1, the lath martensite has the unique hierarchical microstructure with high dislocation density and the mechanical properties are closely related to the microstructure evolution. From these facts, the purpose of this study is to characterize the microstructure of lath martensite phase by means of simulation and experiments.

In terms of simulation, the martensitic transformation in Fe-0.1C mass% lath martensitic steel is simulated by the elasto-plastic phase-field model based on the two types of slip deformation (TTSD) model. The establishment of this model is to prove the validity of the TTSD model on explaining the formation of lath martensite. On the other hand, the microstructure evolution of lath martensite is presented in 3-D space by the phase-field simulation. Moreover, the maximum dislocation density of lath

martensite phase in Fe-0.1C mass% steel is estimated from the simulation results based on the TTSD model.

In terms of experiments, the dislocation densities in 10Cr–5W low–carbon steels that containing the carbon content with 0.02C, 0.03C, 0.09C and 0.13C mass% were determined by the X-ray line analysis based on the modified Williamson–Hall and Warren–Averbach methods. Moreover, the dependence of the dislocation density on carbon content in lath martensite steels is clarified. Additionally, the microstructure of lath martensite in Fe-9Cr- (0.1, 0.2 and 0.4) C mass% steels were characterized by the the electron back scattered diffraction pattern (EBSP) on scanning electron microscopy (SEM). The refinement of the microstructures of lath martensite with the increase of carbon content is verified.

1.3 Organization of the thesis

On the basis of the background and purposes of the present study, this thesis is organized with six chapters. The summarized contents of each chapter are given below.

In Chapter 1, the background of lath martensite phase and the phase-field method is introduced briefly. Moreover, the purposes and organization of the thesis are also explained in this chapter.

In Chapter 2, the elasto-plastic phase-field model is constructed based on the TTSD model to simulate the formation of lath martensite. The morphological evolution of lath martensite in Fe-0.1C mass% steel is presented in 3-D space by the

phase-field simulation.

In Chapter 3, the maximum dislocation density of the lath martensite phase in Fe-0.1C mass% steel is estimated by the simulation results based on the TTSD model.

In Chapter 4, the dislocation densities in 10Cr–5W low–carbon steel that containing carbon content with 0.02C, 0.03C, 0.09C and 0.13C mass% are determined by X-ray line analysis based on the modified Williamson–Hall and Warren–Averbach methods.

In Chapter 5, the morphology of lath martensite phase in Fe-9Cr-(0.1, 0.2 and 0.4)C mass% steels are characterized by the optical microscopy (OM) and the the electron back scattered diffraction pattern (EBSP) on scanning electron microscopy (SEM) technique.

In Chapter 6, a general conclusion obtained from the present study is summarized.

References

1-1. Y. Wang, A.G. Khachaturyan, Acta Mater. 45 (1997) 759-773.

1-2. P.M. Kelly, J. Nutting, Proc. R. Soc. Lond., Ser. A, Math. Phys. Sci. 259 (1960) 45-58.

1-3. T. Maki, I. Tamura, Tetsu-to-Hagane. 67 (1981) 852-866.

1-4. Y. Tomita, T. Iwamoto, Int. J. Mech. Sci. 43 (2001) 2017-2034.

1-5. V.I. Levitas, A.V. Idesman, D.L. Preston, Phys. Rev. Lett. 93 (2004) 105701.

1-6. Z. Nishiyama, Academic press inc. New York (1978).

1-7. F. Falk, Z. Physik B-Condensed Matter. 51 (1983) 177-185.

1-8. G.R. Barsh, J.A. Krumhansl, Phys. Rev. Lett. 53 (1983) 1069-1072.

1-9. A.E. Jacobs, Phys. Rev. B. 52 (1995) 6327-6331.

1-10. X.Y. Song, N.J. Gu, ISIJ Int. 36 (1996) 592-594.

1-11. S. Morito, H. Tanaka, R. Konishi, T. Furuhara, T. Maki, Acta Mater. 51 (2003) 1789-1799.

1-12. A. Shibata, A. Shibata, S. Morito, T. Furuhara, T. Maki, Acta Mater. 57 (2009) 483-492.

1-13. S. Morito, H. Tanaka, R. Konishi, T. Furuhara, T. Maki, Acta Mater. 51 (2003) 1789-1799.

1-14. H. Kitahara, R. Ueji, N. Tsuji, Y. Minamino, Acta Mater. 54 (2006) 1279-1288.

1-15. A.R. Marder and G. Krauss, ASM Trans. Q. 62 (1969) 957-964.

1-16. K. Iwashita, Y. Murata, Y. Tsukada, T. Koyama, Philos. Mag. 91 (2011) 4495-4513.

1-17. A.G. Khachaturyan, *Theory of Structural Transformations in Solids*, New York: John Wiley and Sons Inc.; 1983.

1-18. P.M. Kelly, A. Jostsons, R.G. Blake, Acta Metall. Mater. 38 (1990) 1075-1081.

1-19. R. Kobayashi, Phys. D 63 (1993) 410-423.

1-20. A. Yamanaka, T. Takaki, Y. Tomita, Mater. Trans. 47 (2006) 2725-2731.

1-21. T. Takaki, T. Hasebe, Y. Tomita, J. Crystal Growth 287 (2006) 495-499.

1-22. Y.W. Cui, T. Koyama, I. Ohnuma, K. Oikawa, R. Kainuma, K. Ishida, Acta Mater. 55 (2007) 233-241.

1-23. K.R. Elder, F. Drolet, J.M. Kosterlitz, M. Grant, Phys. Rev. Lett. 72 (1994) 677-680.

1-24. Y. Kondoh, M. Yoshizawa, A. Nakano, T. Yabe, Phys. Rev. E. 54 (1996) 3017-3020.

1-25. J.A. Warren, W.J. Boettinger, Acta Metall. Mater. 43 (1995) 689-703.

1-26. A.A. Wheeler, W.J. Boettinger, G.B. McFadden, Phys. Rev. E. 47 (1993) 1893-1909.

1-27. Y. Wang, L.Q. Chen, A.G. Khachaturyan, Acta Metall. Mater. 41 (1993) 279-296.

1-28. L.Q. Chen, Scripta Metall. Mater. 32 (1995) 115-120.

Chapter 2

Microstructure Simulation of Lath Martensite Phase by Elasto-Plastic Phase-Field Model

2.1 Introduction

It is well known that the mechanical properties of steels are strongly affected by the morphology of martensite phase. In ferrous alloys, various morphologies of the martensite phase, such as thin plate, lenticular, and lath martensite, can be observed with different chemical compositions **[2-1, 2-2]**. Among them, lath martensite is important for heat-resistant steels, because the carbon content in the recent heat-resistant steels is about 0.1 mass%, and the martensite phase formed in such steels is lath martensite. Lath martensite has a hierarchical structure consisting of packets, blocks, and laths containing densely packed complex and tangled dislocations without twins **[2-3]**. Change in high-temperature strength of heat-resistant steels with creep time depends on the microstructural evolution of steels at elevated temperatures. Thus, it is important to clarify the formation process and evolution process of the hierarchical structure in lath martensite. Recently, Iwashita et al. **[2-4]** clarified the formation mechanism of lath martensite by presenting two types of slip deformation (TTSD) model by extending Khachaturyan's slip deformation model.

The phase-field (PF) method has been extensively studied as a powerful tool to investigate various microstructural evolutions, such as the austenite to ferrite transformation, the ferrite-pearlite phase, dendritic patterns, and martensitic textures

[2-5~2-11]. In particular, Khachaturyan et al. integrated microelasticity into the phase-field theory. The resulting model is known as the phase-field microelasticity (PFM) model to simulate the martensitic transformation **[2-12~2-15]**. All these studies are concerned with the elastic strain induced by the phase transformation. However, they omit the effects of the transformation dislocations, which offer plastic accommodation to relax the very large lattice strain introduced by Bain deformation. The dislocation slip results in the irreversible plastic changes in the solid phase. In other words, most of this work focuses on the simulation of twin martensite **[2-16]**.

The purpose of this chapter is to construct a new phase-field model considering dislocation deformation for the plastic accommodation in martensitic transformation. From this purpose, an elasto-plastic phase-field model is developed based on the TTSD model in 3-D space.

2.2 Two types of slip deformation (TTSD) model

In the model proposed by Iwashita et al. **[2-4]**, the formation mechanism of lath martensite phase is described by the two types of slip deformation (TTSD) model. In this model, the crystal deformation for martensitic transformation is realized by coupling the lattice deformation described by Bain deformation and plastic deformation by two types of dislocation slips. With the assistance of TTSD model, the habit plane $(557)_{\gamma}$ and lattice correspondence between the martensite phase and the austenite phase are exactly explained without any rotation matrix for the Bain deformation as explained in the following sections in this chapter.

2.2.1 Lattice deformation

The lattice deformation is characterized by Bain deformation **[2-17]**. To generate the Bain deformation, a tetragonal cell is set in two face center cubic (*fcc*) crystal cells of the austenite phase as shown in Fig. 2-1 (a). The body center tetragonal (*bct)* martensite lattice is obtained from the tetragonal cell by Bain deformation as shown in Figs. 2-1 (b) and (c). For the case shown in Fig. 2-1, the $[001]_{\gamma}$ axis coincides with $[001]_{\alpha'}$. Hereafter, the subscript γ represents the austenite phase and α' indicates the martensite phase. The other two cases where the $[100]_{\gamma}$ axis coincides with $[001]_{\alpha'}$ and the $[010]_{\gamma}$ axis coincides with $[001]_{\alpha'}$ are treated in a similar manner as the case shown in Fig. 2-1. Thus, the three different blocks in a packet of lath martensite phase are formed due to the three cases of lattice cooresponding .

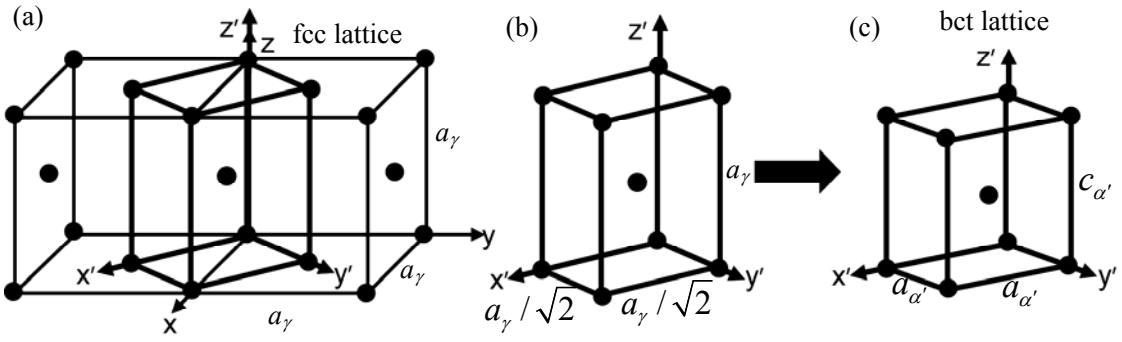

Fig. 2-1 Skeleton of Bain deformation from *fcc* to *bct* crystal lattice.

2.2.2 Plastic deformation

The elastic strain energy caused by Bain deformation is so large that plastic

deformation is inevitable. According to the two types of slip deformation (TTSD) model **[2-4]**, the plastic accommodation is realized by two independent slip systems. For simplicity, just the case where the $[001]_{\gamma}$ axis coincides with the $[001]_{\alpha'}$ is explained here as a representative example. After the Bain deformation, the length of the *c*-axis in the bct martensite lattice are adjusted properly to release the strain energy caused by the Bain deformation. In this simulation, it is assumed that the plastic deformation is totally accommodated by dislocations slip along the two slip systems **[2-16]**, i.e., $[101](\bar{1}01)_{\alpha'}$ and $[\bar{1}01](101)_{\alpha'}$ as shown in Fig. 2-2 (a). Each slip system can be taken as a combination of two $a/2\langle 111\rangle_{\alpha'}$ dislocation slips with the Burgers vectors $\mathbf{b_1}$ and $\mathbf{b_2}$ as shown in Fig. 2-2 (b). In fact, it has been reported that densely packed $a/2\langle 111\rangle_{\alpha'}$ dislocations always exist in commercial steels **[2-18]**. The crystal orientation between lath martensite and austenite phase obeys the KS **[2-19]** relationship, resulting in the 24 crystallographic orientation, i.e., lath variants in lath martensite, which has been explained explicitly in Chapter 1. In the present simulation, we only treat the six variants in a packet of lath martensite, i.e., V1~V6 as shown in Table 1-1. The six variants in a packet have different direction parallel relationships on the same closed packed plane, which is representative for the microstructure in lath martensite. As mentioned previously, there are three blocks in each packet due to the three cases of lattice correspondence. For the plastic deformation, each block has two evolution paths, i.e., the two types of slip systems, resulting in the formation of six variants in a packet, i.e., V1, V2, V3, V4, V5, and V6. It is reported that the six crystallographic variants in a packet always appear in pairs and the two variants in

each pair with the similar crystal orientation. This is the so-called sub-block structure of lath martensite. With the assistance of the TTSD model, lath martensite phase with a sub-block microstructure can be formed.

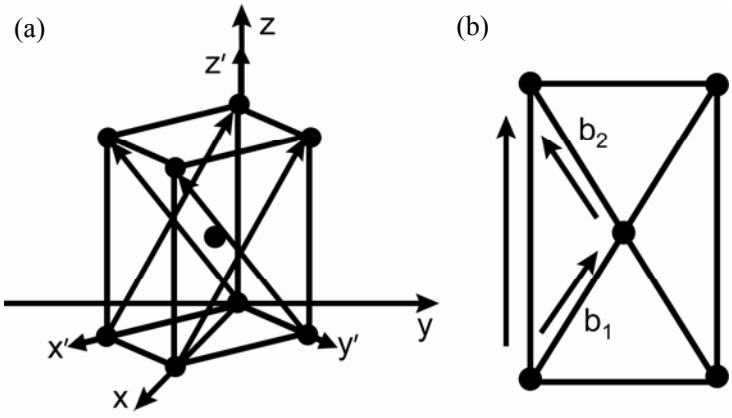

Fig. 2-2 Skeleton of plastic deformations by the two slip systems when the $[001]_{\gamma}$ axis coincides with $[001]_{\alpha'}$. The two crossed planes represent two-slip systems, i.e., $[101](\bar{1}01)_{\alpha'}$ and $[\bar{1}01](101)_{\alpha'}$.

2.3 Elasto-plastic phase-field model

By coupling the phase-field method with the TTSD model, an elasto-plastic phase-field model is constructed to simulate the formation of lath martensite. For phase-field model, a long range order (LRO) field variable $\phi_i(\mathbf{r})(i=1,2,3)$ is introduced to describe the Bain deformation. $i=1,2,3$ is used to distinguish the three cases of lattice corresponding in Bain deformation and **r** is the coordinate vector. $\phi_i(\mathbf{r})$ is between 0 to 1 and 0 represents the disordered phase (austenite), while 1 is the ordered phase (martensite) as shown in Fig. 2-3.

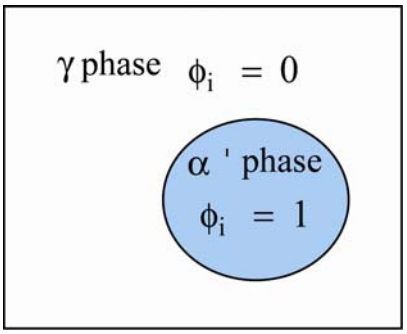

Fig. 2-3 Schematics of the LRO field variable, which assumes that 1 is the ordered phase, and 0 is the disordered phase.

The eigen strain caused by the Bain deformation $\varepsilon_{kl}^{B}(i)(i=1,2,3)$ is listed in matrix form as

$$\varepsilon_{kl}^{B}(1)=\begin{pmatrix}\sqrt{2}a_{\alpha'}/a_{\gamma}-1 & 0 & 0\\ 0 & \sqrt{2}a_{\alpha'}/a_{\gamma}-1 & 0\\ 0 & 0 & c_{\alpha'}/a_{\gamma}-1\end{pmatrix}, \tag{2-1}$$

$$\varepsilon_{kl}^{B}(2)=\begin{pmatrix}c_{\alpha'}/a_{\gamma}-1 & 0 & 0\\ 0 & \sqrt{2}a_{\alpha'}/a_{\gamma}-1 & 0\\ 0 & 0 & \sqrt{2}a_{\alpha'}/a_{\gamma}-1\end{pmatrix}, \tag{2-2}$$

$$\varepsilon_{kl}^{B}(3)=\begin{pmatrix}\sqrt{2}a_{\alpha'}/a_{\gamma}-1 & 0 & 0\\ 0 & c_{\alpha'}/a_{\gamma}-1 & 0\\ 0 & 0 & \sqrt{2}a_{\alpha'}/a_{\gamma}-1\end{pmatrix}, \tag{2-3}$$

where a_{γ} is the lattice parameter of the austenite phase, $a_{\alpha'}$ and $c_{\alpha'}$ are the lattice parameters of the martensite phase, respectively.

With respect to the plastic deformation, it is realized by dislocation slips. In the phase-field model of dislocations, the deformed region sheared by a dislocation loop is described as a plate with thickness equal to the interplanar spacing of the glide planes **[2-20]**. By extending this description to a spatial region containing dislocations

to characterize the plastic deformation, the eigen strain can be written as $\varepsilon^p(x)=\sum_{\alpha=1}^{p}\frac{\mathbf{b}_\alpha\otimes\mathbf{n}_\alpha+\mathbf{n}_\alpha\otimes\mathbf{b}_\alpha}{2D_\alpha(x)}$, where p is the total number of slip systems and $D_\alpha(x)$ is the average distance between neighboring slip planes. Then a new set of field variable $p_i^\alpha(\mathbf{r})(i=1,2,3)$ is introduced **[2-21]**

$$p_i^\alpha=\frac{\left|\mathbf{b}_i^\alpha\right|}{D_i^\alpha}(i=1,2,3)\,, \tag{2-4}$$

which characterizes the values of local plastic strain produced by dislocations from a specific slip system. α is the number of active slip systems. When α is equal to 1 and 2, it corresponds to the slip system $[101](\bar{1}01)_{\alpha'}$ and $[\bar{1}01](101)_{\alpha'}$, respectively, when $i=1$, i.e., a case of lattice corresponding in the Bain deformation. Therefore, the eigen strain tensor ε_{kl}^P, caused by plastic deformation can be given by

$$\varepsilon_{kl}^P=\sum_{\alpha=1,2}\frac{\mathbf{b}_i^\alpha\otimes\mathbf{n}_i^\alpha+\mathbf{n}_i^\alpha\otimes\mathbf{b}_i^\alpha}{2\left|\mathbf{b}_i^\alpha\right|}\cdot p_i^\alpha(\mathbf{r})(i=1,2,3)\,, \tag{2-5}$$

where $\mathbf{b}_i^\alpha$ is the Burgers vector, $\mathbf{n}_i^\alpha$ is the unit vector of the slip plane normal, the subscript *P* represents plastic deformation and $\otimes$ represents the dyadic product. In Eq. (2-4), the denominator can also be expressed as

$$D_i^\alpha=m_i^\alpha\times d_{hkl}\,, \tag{2-6}$$

where m_i^α is the number of lattice planes between neighboring slip planes in each slip system, and d_{hkl} is the distance of each $(hkl)_{\alpha'}$ plane. Due to the existence of two types of slip systems, there will be a pair of slip deformation p_i^α for each lattice correspondence (*i*), resulting in a pair of *m*, i.e., m_1 and m_2 to distinguish the two

independent slip systems according to Eqs. (2-4) and (2-6). Here, the subscripts 1 and 2 correspond to the $[101](\bar{1}01)_{\alpha'}$ and $[\bar{1}01](101)_{\alpha'}$ slip system, respectively, for a certain lattice correspondence.

Three different blocks in a packet are generated due to the Bain deformation, which correspond to the three cases of lattice corresponding. In our simulation, the different blocks come from the different Bain deformation. While the two variants in each blocks have the same Bain deformation but different plastic deformation.

2.3.1 Energy description of martensitic transformation

The martensitic transformation is a minimization process of the total free energy described by the elasto-plastic phase-field model. For a structurally non-uniform system, the total free energy F_{total}, is defined as the sum of the chemical energy, the gradient energy and the elastic strain energy:

$$F_{total} = \int_{\mathbf{r}} \left[f_L + E_{grad\_\phi} + E_{grad\_p} + E_{el} \right] d\mathbf{r} , \tag{2-7}$$

where f_L is specific local free energy density, E_{grad_ϕ} and E_{grad_p} are the gradient energy density with respect to the field variable $\phi_i(\mathbf{r})$ and p_i^{α}, respectively, and E_{el} is the elastic energy density caused by a coherent interface.

f_L is the specific free energy, which is invariant with respect to any rotation and symmetries of austenite phase and it follows the Landau polynominal expansion as **[2-15]**:

$$f_L = \Delta f \left\{ \frac{a}{2}(\phi_1^2 + \phi_2^2 + \phi_3^2) - \frac{b}{3}(\phi_1^3 + \phi_2^3 + \phi_3^3) + \frac{c}{4}(\phi_1^2 + \phi_2^2 + \phi_3^2)^2 \right\} \quad . \qquad (2\text{-}8)$$

Here, *a*, *b*, and *c* are dimensionless coefficients of the Landau polynomial expansion. The symmetry of Eq. (2-8) results in the automatic degeneration of the global minimum in the space of the $\{\phi_i\}$ variables into a set of three $(i = 1, 2, 3)$ equal global minima. Each of these minima describes the corresponding domain of lath martensite, i.e., ϕ_1, ϕ_2 and ϕ_3. In this study, the dimensionless coefficients are chosen as $a = 0.1$, $b = 3a + 12$, and $c = 2a + 12$ to provide a local minimum at $\phi_1 = \phi_2 = \phi_3 = 0$. Δf is the driving force for the martensitic transformation, which is equal to the chemical free energy difference between the austenite and martensite phases. Δf is calculated by Thermo-Calc with CALPHAD method **[2-22]**. Fig. 2-4 **[2-15]** shows the specific free energy f_L when $\phi_2 = \phi_3 = 0$, which reveals that the local minimum at $\phi_1 = 0$ represents a metastable state, while the absolute minimum $\phi_1 = 1$ corresponds to an equillibrium state for the martensite phase. The difference of the free energy between these two state is the driving force for martensitic transformation. This driving force influences the width of austenite/martensite interface, λ. With the increase of driving force, λ decreases, resulting in the interface become sharp. The local maxima describes the chemical energy barriers of the transformation, which provides the energy hump between the austenite phase and martensite phase.

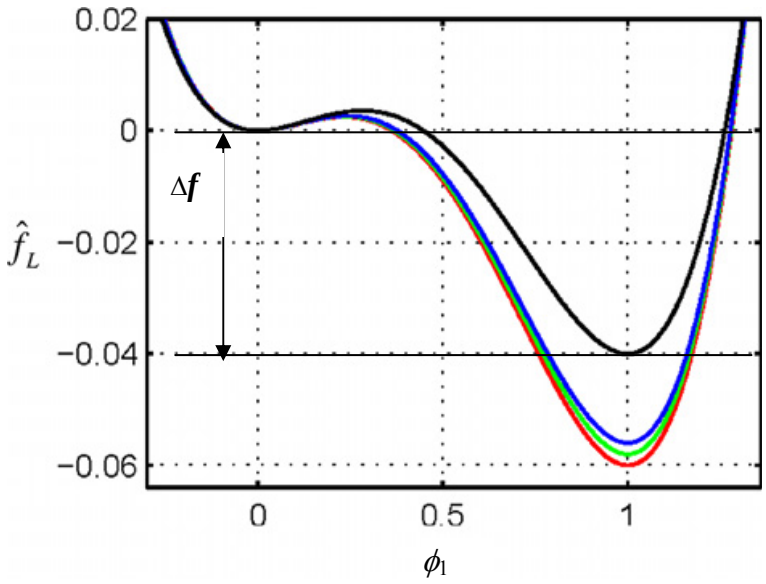

Fig. 2-4 Landau energy density for $\phi_2 = \phi_3 = 0$ quotoed from *Ref*. **[2-15]**.

According to gradient thermodynamics **[2-23~2-25]**, the gradient energy density E_{grad_ϕ} accounts for contributions from spatial variation of $\phi_i(\mathbf{r})$ and is given by

$$E_{grad\_\phi} = \frac{\kappa_\phi}{2}\sum_{i=1}^{3}(\nabla\phi_i(\mathbf{r}))^2 . \tag{2-9}$$

κ_ϕ is the gradient energy coefficient with respect to $\phi_i(\mathbf{r})$, which can be determined by fitting interfacial energies to experimental or calculated data **[2-26]**. The value of κ_ϕ also affects the width of interface λ, which increases with the increase of gradient coefficient, resulting in the interface becomes diffuse. $\nabla \equiv \partial / \partial r_i$ is a differential operator. In fact, the gradient energy E_{grad_ϕ}, reflects the interfacial energy.

The gradient energy density E_{grad_p} with respect to p_i^α is given by **[2-21]**

$$E_{grad\_p} = \frac{\kappa_p}{2}\sum_{i=1}^{3}\sum_{\alpha=1,2}\left[\mathbf{n}_i^\alpha \times \nabla p_i^\alpha(\mathbf{r})\right]\cdot\left[\mathbf{n}_i^\alpha \times \nabla p_i^\alpha(\mathbf{r})\right], \tag{2-10}$$

where κ_p is the gradient energy coefficient that guarantees a smooth transition of the deformation strain field profile on the austenite/martensite interface. Eq. (2-10) describes the gradient energy attributed to the core energy of the dislocations to the plastic accommodation, which corresponds to the geometrically necessary dislocations described by Ashby's model.

In forming a coherent interface where the atomic lattice planes are continuous from one domain to another, the lattices in both domains are necessarily distorted to accommodate their mismatch at interface. Such accommodation reduces the interfacial energy, while causes the elastic energy stored in all domains. The elastic energy density is derived as **[2-16, 2-27]**,

$$E_{el} = \frac{1}{2}\boldsymbol{C_{ijkl}}\left\{\varepsilon_{ij}(\mathbf{r}) - \varepsilon_{ij}^{0}(\mathbf{r})\right\}\left\{\varepsilon_{kl}(\mathbf{r}) - \varepsilon_{kl}^{0}(\mathbf{r})\right\}, \qquad (2\text{-}11)$$

where $\boldsymbol{C_{ijkl}}$ is the elastic modulus tensor. In a real case, the elastic strain energy also comes from the deformed austenite phase. So the elastic constants of austenite phase should be used to estimate the strain energy. However, in the present simulation, it is assumed that all of the elastic strain comes from the lath martensite during phase transition due to the complexity of considering the deformed austenite phase. In this assumption, the strain from the deformed austenite phase is contained in the total elastic strain estimated by Eq. (2-11). After such assumptions, the elastic constants of martensite phase should be adopted for calculation. But there are lack of the experimental results of the elastic constants for martensite up to now, for simplicity, the isotropic elasticity is used in this calculation. And thus the tensor $\boldsymbol{C_{ijkl}}$ **[2-14]** can

be expressed as $\boldsymbol{C_{ijkl}} = \lambda\delta_{ij}\delta_{kl} + \mu(\delta_{ik}\delta_{jl} + \delta_{il}\delta_{jk})$ in terms of the Lamé constants λ and μ in a pure iron. $\delta(x)$ is the Kronecker delta function. The total eigen strain $\varepsilon_{kl}^{0}(\mathbf{r})$ is the sum of Bain strain $\varepsilon_{kl}^{B}(i)$, and eigen strain for plastic deformation ε_{kl}^{P}, which is shown as below:

$$\varepsilon_{kl}^{0} = \sum_{i=1}^{3}[\left(\varepsilon_{kl}^{B}(i)\cdot\phi_i(\mathbf{r})\right) + \sum_{\alpha=1,2}\frac{\mathbf{b}_i^{\alpha}\otimes\mathbf{n}_i^{\alpha} + \mathbf{n}_i^{\alpha}\otimes\mathbf{b}_i^{\alpha}}{2\left|\mathbf{b}_i^{\alpha}\right|}\cdot p_i^{\alpha}(\mathbf{r})]. \tag{2-12}$$

$\varepsilon_{kl}(\mathbf{r})$ in Eq. (2-11) is the total strain, which is defined as the sum of the homogeneous strain $\bar{\varepsilon}_{kl}$ and the heterogeneous strain $\delta\varepsilon_{kl}$:

$$\varepsilon_{kl}(\mathbf{r}) = \bar{\varepsilon}_{kl} + \delta\varepsilon_{kl}(\mathbf{r}). \tag{2-13}$$

The homogeneous strain is a uniform macroscopic strain and describes the macroscopic deformation of the system, which is given by $\bar{\varepsilon}_{kl} = 1/V\int_{\mathbf{r}}\varepsilon_{kl}^{0}(\mathbf{r})d\mathbf{r}$, where V is the total volume of the system. The heterogeneous strain is expressed as **[2-28]**

$$\delta\varepsilon_{kl}(\mathbf{r}) = \frac{1}{2}\left\{\frac{\partial u_k(\mathbf{r})}{\partial r_l} + \frac{\partial u_l(\mathbf{r})}{\partial r_k}\right\}, \tag{2-14}$$

where u_k represents the kth component of the elastic displacement. By using the local equilibrium equation, namely $\partial\sigma_{ij}^{el}/\partial r_j = 0$, the heterogeneous dislplacement in Fourier space can be solved. Finally, the heterogeneous strain is given by

$$\delta\varepsilon_{kl}(\mathbf{r}) = \frac{1}{2}\left\{\Omega_{ik}(\mathbf{k})n_l + \Omega_{il}(\mathbf{k})n_k\right\}C_{ijpq}\varepsilon_{pq}^{0}n_j, \tag{2-15}$$

where $\Omega_{ik}(\mathbf{k})$ is the Green function tensor.

Both of the field variable $\phi_i(\mathbf{r})$ and $p_i^{\alpha}(\mathbf{r})$ are taken as non-conserved fields because they have no kinematic constrains and their values are determined by the free energy minimization only. Therefore the temporal dependence follows the general Time Dependent Ginzburg-Landau (TDGL) kinetic equation **[2-12, 2-20]**:

$$\frac{\partial M(\mathbf{r},t)}{\partial t} = -L_M \frac{\delta F_{total}}{\delta M(\mathbf{r},t)}, \tag{2-16}$$

where $M(\mathbf{r},t)(M = \phi_i, p_i^{\alpha})$ are the field variables and $L_M(M = \phi_i, p_i^{\alpha})$ are the kinetic parameters, which reflect the diffusion mobility of each specific field. The negative sign indicates that the evolution is driven to the energy minimum. The mobility for the microstructure evolution is determined by the relationship between the kinetic parameters L_{ϕ} and L_p. In the TTSD model, the slip deformation should follow the Bain deformation. However, in real materials, the dislocations assiting the plastic accommodation move so fast during martensitic transformation. So it is assumed that the mobility of the dislocation field and the interface is the same to each other, i.e., $L_{\phi} = L_p$, to guarantee that the process of microstructure evolution is diffusion-controlled.

2.3.2 Numerical simulation

The martensitic transformation in Fe-0.1C mass % steel was simulated at 300K in 3-D space by the phase-field model. Eq. (2-16) is solved by a finite difference method with the periodic boundary conditions. The transformation is calculated numerically with the Fast Fourier Transformation (FFT) method according to the phase-field

microelastisity **[2-16]**. The simulation was performed in a cubic with N^3 (N=64) grid points. Such scale is chosen because the size effect and the inaccuracy introduced by the assumption of macroscopic homogeneity, which are both associated with the comparatively small system volume, are not too significant to prevent reproducing the major features of the martensitic structures. The size of each grid, refered to as the length scale, has two particular constrains in the phase field model. The first is to be large enough that a moderate number of grids can span the entire microstructure, but be fine enough that a diffuse interface can be maintained. In this study, the grid size l is calculated to be 4 nm by fitting the interfacial energy. Therefore, the computational domain is 256 × 256 × 256 nm.

For the initial state, a dislocation loop was set in the center of a homogeneous austenite crystal with a radius of 12 nm and thickness. This dislocation loop introduces a stress-free strain, which is given by a symmetric dyadic product of $\mathbf{b}_1 = \frac{1}{2} a_\gamma [\bar{1}10]$ and the unit vector $\mathbf{n}_1 = \left\langle 1/\sqrt{3}, 1/\sqrt{3}, 1/\sqrt{3} \right\rangle$ as $\varepsilon_{ij}^d(1) = \frac{\mathbf{b}_1 \otimes \mathbf{n}_1 + \mathbf{n}_1 \otimes \mathbf{b}_1}{2d_{(111)}}$, where $d_{(111)} = a_\gamma / \sqrt{3}$ is the interplanar distance. The simulation parameters used in the present model are listed in Table 1. For an isotropic calculation system, the Lamé constants λ and μ are estimated from the Young's modulus and the Bulk modulus in pure iron **[2-29]**. The gradient coefficient κ_ϕ is fitted to the interfacal energy per area, $\gamma = 0.01 J/m^2$, calculated from TEM data **[2-16]**, ensuring a coherent boundary between the domain walls.

For convenience of numerical simulation, the physical parameters are converted to dimensionless quantities. The length is scaled by the grid size l and all the

energies are scaled by RT, where R is the gas constant, T is the absolute tempreture. The kinetic paramenters $L_M(M=\phi_i, p_i^\alpha)$ are set to as $L_M^* = 1$ to guarantee the diffusion controlled microstructure evolution, where the asterisk denotes a dimensionless quantity. The unit time step is selected as $\Delta t^* = 0.001$ to maintain numerical accuracy and stability.

Table 2-1 Simulation parameters for the phase-field model in Fe-0.1C mass % steel

Lattice parameters, a (m)	$a_\gamma = 3.599\times10^{-10}$, $a_{\alpha'} = 2.867\times10^{-10}$, $c_{\alpha'} = 2.880\times10^{-10}$
Elastic constants, C_{ijkl} (Gpa)	$C_{11} = 267$, $C_{12} = 123$, $C_{44} = 72$
Gradient coefficients, ($J\cdot m^2/mol$)	$\kappa_\phi = 1.6\times10^{-14}$, $\kappa_p = 30\times10^{-14}$
Driving force, Δf (J/mol)	5085
Tempreture, T (K)	300

2.4 Results and discussion

Fig. 2-5 shows the simulation result of the initial state of lath martensite, which is a circular platelet as shown in (a) and the platelet is with some a thickness as shown in (b) observed from another view angle.

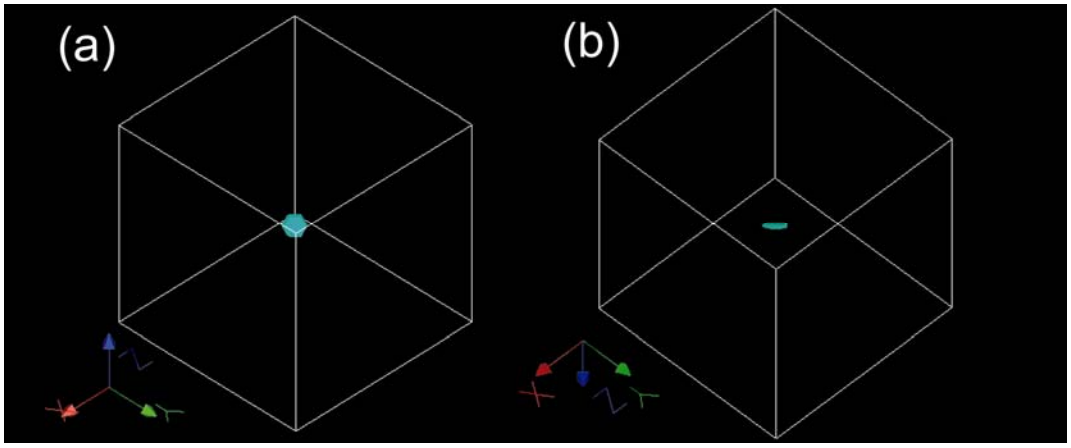

Fig. 2-5 Simulation result of the initial state of lath martensite. (a) and (b) are the same state observed from different view angles in 3-D space.

Fig. 2-6 shows the simulation result of time evolution of energy densities in Fe-0.1C mass% steel. It was observed that the elastic energy density and gradient energy density increase monotonically, while the specific free energy density decreases monotonically with time t^* from about 4600 to 0 *J/mol*. It is also observed that the gradient energy coming from the interface is much bigger than that attributed to the dislocation core energy. The specific free energy is the driving force for martensitic transformation to overcome the increase of the sum of elastic energy and gradient energy resulting in the minimization of total free energy. It is noted that all energy densities have become steady around 20 time steps, indicating the end of martensitic transformation. It should be noted that even though the growth of the martensite phase is mostly driven by the chemical free energy, the refining and coalescence of the microstructure are driven by the strain energy and the gradient energy reduction.

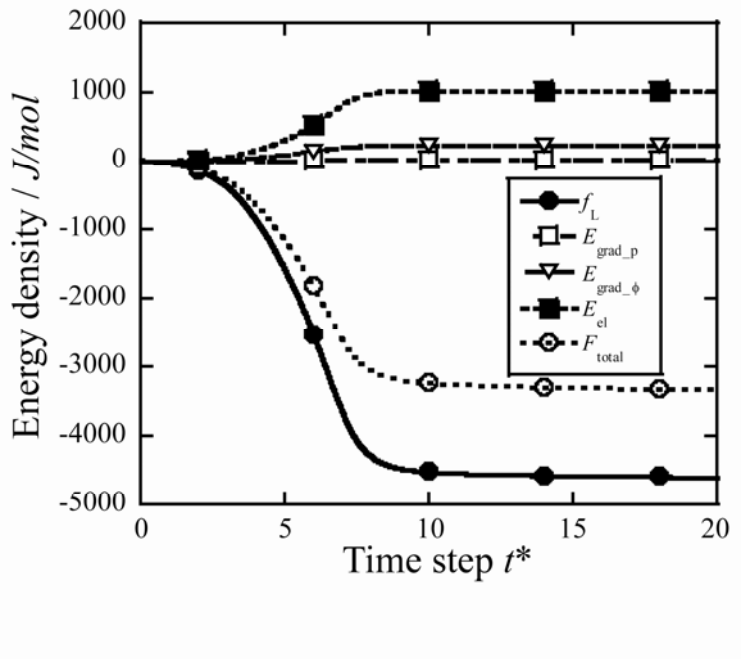

Fig. 2-6 Simulation result of time evolution of energy densities in Fe-0.1C mass% steel at 300K.

Fig. 2-7 shows the simulation result of time evolution of three types of blocks in a packet on the {111} plane. The blue areas represent the retained austenite phase and the other colored areas (green, yellow, and red) represent three different blocks as explained in the formation mechanism of lath martensite. The occurrence of each block is determined by the value of the field variable $\phi_i(\mathbf{r})$. In this simulation, it is assumed that the martensite phase appears only when $\phi_i(\mathbf{r}) \geq 0.7$. As shown in Fig. 2-7 that at $t^* = 2$, all of the three blocks appear around the dislocation loop set in the center of simulation region. At $t^* = 4$, different blocks grow bigger around the existing martensite phase. In the process of martensite growth, when a second order block meets a first order block, it will stop growing. It results in that the boundary of the first order block is a straight line. In this manner, the martensite phase becomes

coarser until the morphology of the full martensite appears. At t^* = 8, the packet is almostly full of lath martensite phase except that only a few austenite phase can be seen. At t^* = 20, the three blocks have accupied the whole simulation region, indicating the accomplishment of the martensitic transformation.

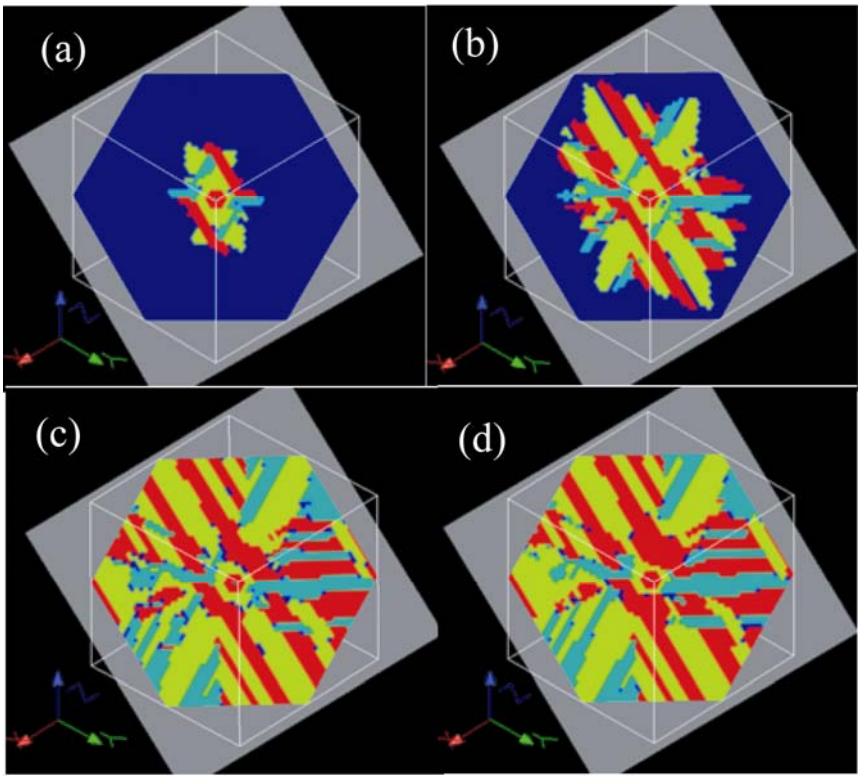

Fig. 2-7 Time evolution of blocks on {111} plane for (a) t^* = 2, (b) t^* = 4, (c) t^* = 8, and (d) t^* = 20 simulated by elasto-plastic phase-field model. The three colors, i.e., blue, red, and yellow represent three blocks and deep blue represents austenite phase.

Fig. 2-8 shows the simulation results of time evolution of lath variants in a packet on the {111} plane and the six colored areas represent the six variants which are illustrated explicitly in (e). As shown in Fig. 2-8 (e), each block shown in Fig. 2-7 is composed of a pair of variants, i.e., V1~V4, V2~V5, and V3~V6, which is the so-called sub-block structure in lath martensite. A block composed of the two

martensitic variants defined by the KS relationship is ideal for the adjustment of plastic deformation by the two types of slip systems. For comparing, the experimental result is shown in (f), which is the EBSP observation of lath martensite **[2-30].** In Fig. (f), the parallel block structure can be observed and each block is a combination of the two variants. By comparing Figs. 2-8 (e) and (f), the qualitative similarity of the sub-block micorostructure between the simulation results and experimental observation can be seen. The ratio of the volume fraction of the three block in our simulation is calculated to be 1:1:1 by the mesh method, while the ratio of B1:B2:B3 in (f) is calculated to be 1:2:1. As the lath martensite is an inhomogeneous system, it needs a lot of mapping information for the accurate quantitative analysis, which is unavailable up to present and needs further effort.

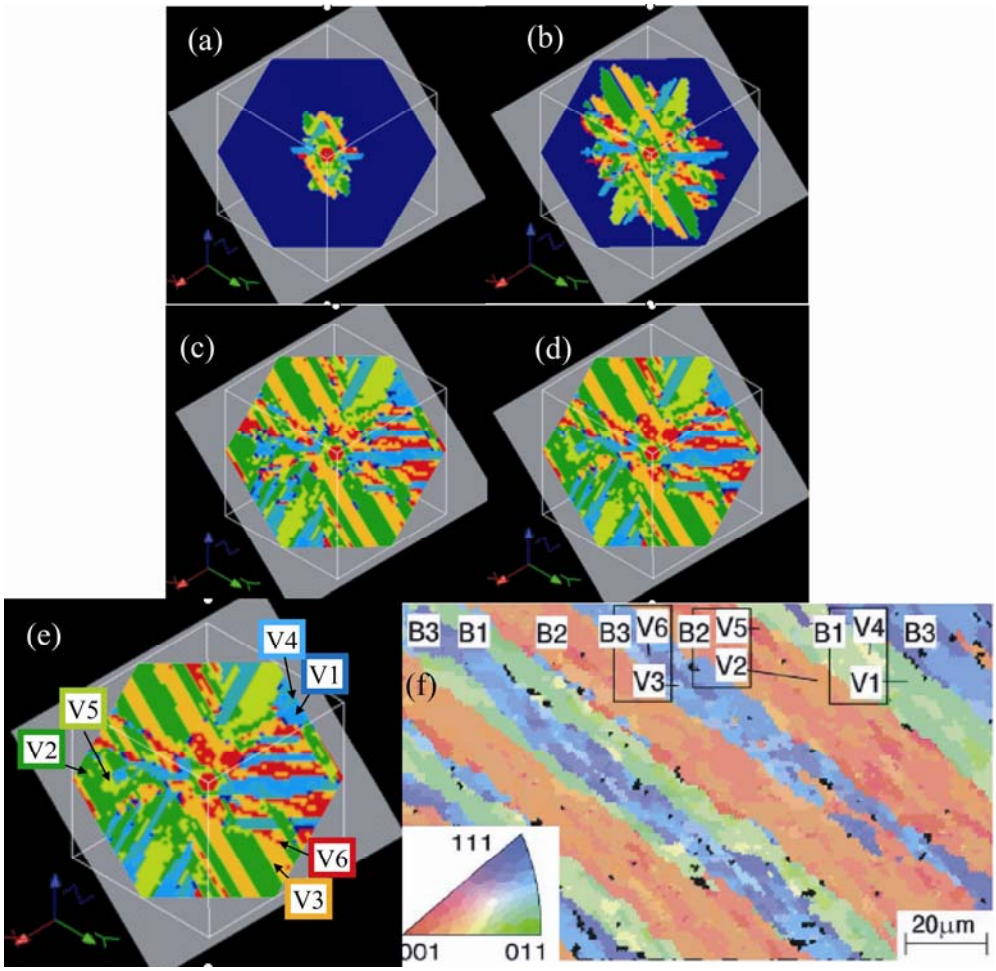

Fig. 2-8 Time evolution of lath variants on {111} plane for (a) $t^* = 2$, (b) $t^* = 4$, (c) $t^* = 8$, and (d) $t^* = 20$ simulated by elasto-plastic phase-field model. (e) is the specific explanation of variants shown in (d). The six colors represent six different variants in a packet. (f) is the EBSP observation of lath martensite quoted from Ref. **[2-30]**.

Figs. 2-9 and 2-10 show the simulation results of the time evolution of plastic strain $p_i^{\alpha}(\mathbf{r})$ along the slip systems of $[101](\bar{1}01)_{\alpha'}$ and $[\bar{1}01](101)_{\alpha'}$ when $i=1$ in a packet, respectively. The blue areas indicate no slip deformation, whereas the red areas represent the most dramatic slip deformation. Each point in Figs. 2-9 and 2-10 represents a local plastic strain for a certain *i*, whereas all the points scattered in the simulation region contain the plastic strain coming from the three cases of lattice corresponding, i.e., $i=1$, 2 and 3. The slip systems $[101](\bar{1}01)_{\alpha'}$ and $[\bar{1}01](101)_{\alpha'}$ correspond to the slip systems when $i=1$ as explained in Chapter 2. These figures reveal that the plastic deformation originated from the center of the austenite phase and the range of the slip deformation extends with the progression of martensitic transformation. By comparing Figs. 2-9 and 2-10, it is found that the plastic deformation along the two slip systems are complementary with each other. Taking area "A" in Fig. 2-9 and area "B" in Fig. 2-10 as an example, the plastic strain in "A" is very large, while there is almost no plastic deformation in the same area along the other slip system, as shown in "B". This phenomena can be observed at all places and times during martensitic transformation. So it is concluded that the slip deformation along the two slip systems cooperate with each other to assist the plastic accommodation. The phenomena that the plastic deformation occurs along the two slip systems alternatively is consistent with the formation mechanism of sub-block structure in lath martensite. It is to be noted that the plastic strain shown in Figs. 2-9 and 2-10 represent only the local values, which should be integrated within the whole crystal to assess the contribution of dislocation slip on plastic accommodation.

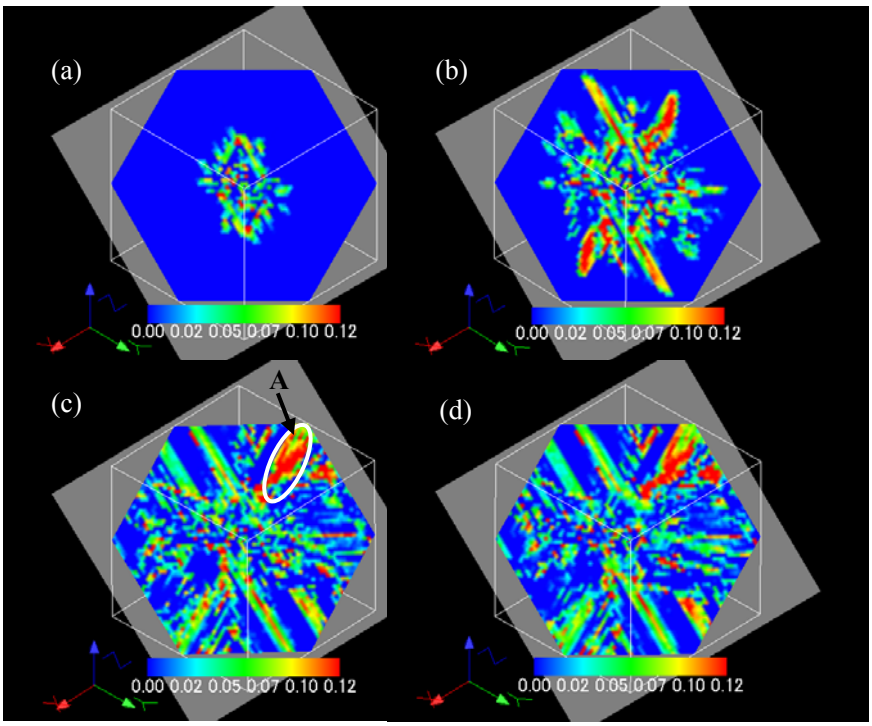

Fig. 2-9 Time evolution of plastic strain $p_i^{\alpha}(\mathbf{r})(i=1,2,3)$ along $[\bar{1}01](101)_{\alpha'}$ slip system on {111} plane for (a) t^* = 2, (b) t^* = 4, (c) t^* = 8, and (d) t^* = 20 by phase-field simulation.

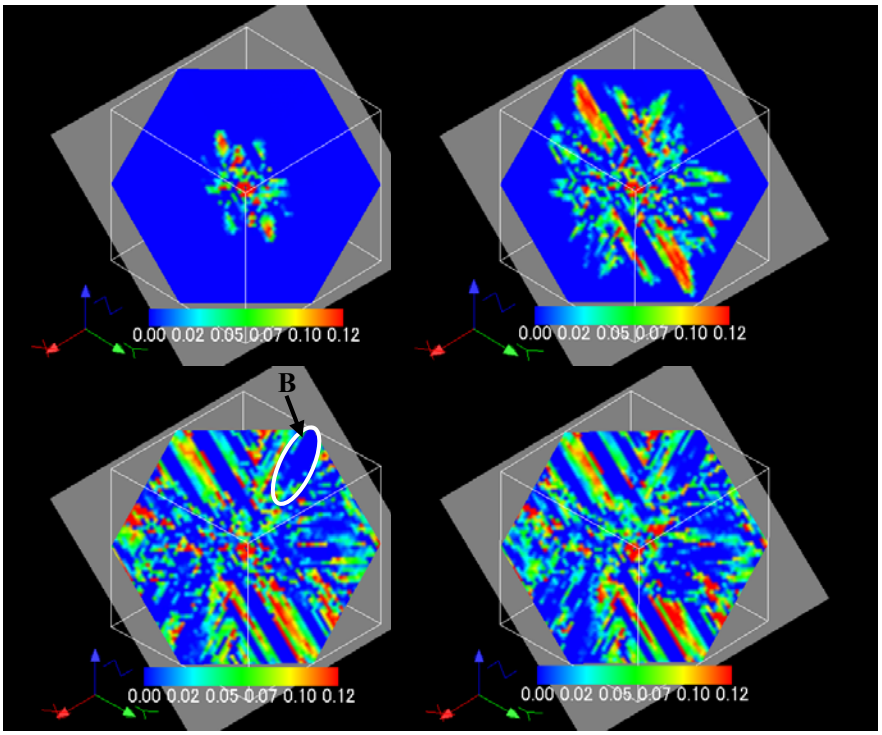

Fig. 2-10 Time evolution of plastic strain $p_i^{\alpha}(\mathbf{r})(i=1,2,3)$ along $[101](\bar{1}01)_{\alpha'}$ slip system on {111} plane for (a) t^* = 2, (b) t^* = 4, (c) t^* = 8, and (d) t^* = 20 by phase-field simulation.

On the other hand, by comparing Fig. 2-8 and Figs. 2-9, 2-10, it is found that the morphology of lath martensitic evolution corresponds to the plastic strain evolution. In particular, the slip deformation in Fig. 2-9 and Fig. 2-10 starts from the beginning of martensitic transformation. With the progression of phase transition, the increase of plastic strain urges the growth and coalescence of the martensitic variants shown in Fig. 2-8. In other words, the occurrence and evolution of the plastic deformation determine the formation and morphological evolution of the lath martensite phase.

By inserting the local plastic strain along each slip system in Eqs. (2-4) and (2-6), the values of m_1 and m_2 can be evaluated. As mentioned previously, the subscripts 1 and 2 correspond to the $[101](\bar{1}01)_{\alpha'}$ and $[\bar{1}01](101)_{\alpha'}$ slip system, respectively, in the lattice corresponding of $i=1$. Because of the three cases of lattice correspondence, there should be three pairs of m_1 and m_2. Since each pair is equivalent, only the case in which the $[001]_{\gamma}$-axis coincides with the $[001]_{\alpha'}$-axis, i.e., $i=1$, is discussed as an example. For this case, the variants of V1 and V4 will appear. For the other two cases, the relationship between the values of m along the two independent slip systems should be similar to that of $i=1$. By inserting the local values of the slip deformation p_1^1 and p_1^2 in Eqs. (2-4) and (2-6), the values of m_1 and m_2 are estimated and the relationship between m_1 and m_2 within simulation areas is plotted in Fig. 2-11 (a), where two thousand local values distributed in the simulation areas are collected. It is found that the dense points concentrate in one corner due to the close values as shown in Fig. 2-11 (a). For easy observation, the m_1 and m_2 maxima are limited to within 100 and the enlarged part is shown in Fig. 2-11

(b). For comparison, the analytical result is also shown in Fig. 2-11 (c), which is obtained from eigenvalues satisfying the invariant plane deformation of the deformation matrix **[2-4]**. A "corner" type contour is exhibited in Fig. 2-11 (b) and the values of m_1 and m_2 in the corner are approximately 16, which is close to the corner point $m_1 = m_2 = 19$ in Fig. 2-11 (c). Fig. 2-11 (b) also reveals that when m_2 reaches its minimum 10, m_1 increases from 20 to infinity. The converse situation yields a similar result. The contour shown in Fig. 2-11 (b) is consistent with the analytical results shown in Fig. 2-11 (c). This indicates that m_1 and m_2 are mutually dependent, which can be seen not only from the analytical results, but also from the simulation results. The relationship between m_1 and m_2 corresponds to the relationship between the plastic deformation along the two slip systems. Therefore, it is concluded that the simulation result of the relationship between the two types of slip deformation is consistent with the analytical solution calculated by the TTSD model. On the other hand, Eqs. (2-4) and (2-6) suggest that if m_1 is larger than m_2, the plastic strain along $[101](\bar{1}01)_{\alpha'}$ is larger than that along $[\bar{1}01](101)_{\alpha'}$. It causes the formation of variant V4. On the contrary, the variant V1 appears. It suggests that the values of m_1 and m_2 determine the appearance of V1 or V4. This simulation result is consistent with the analytical result calculated by Iwashita *et al*. **[2-4]**.

The simulation result of the time evolution of elastic strain energy is plotted in Fig. 2-12. The red colour represents the maximum value of the elastic strain energy and the blue color the minimum value, i.e., when the elastic strain energy is zero. At the initial stage of the martensitic transformation, the elastic strain energy is small as

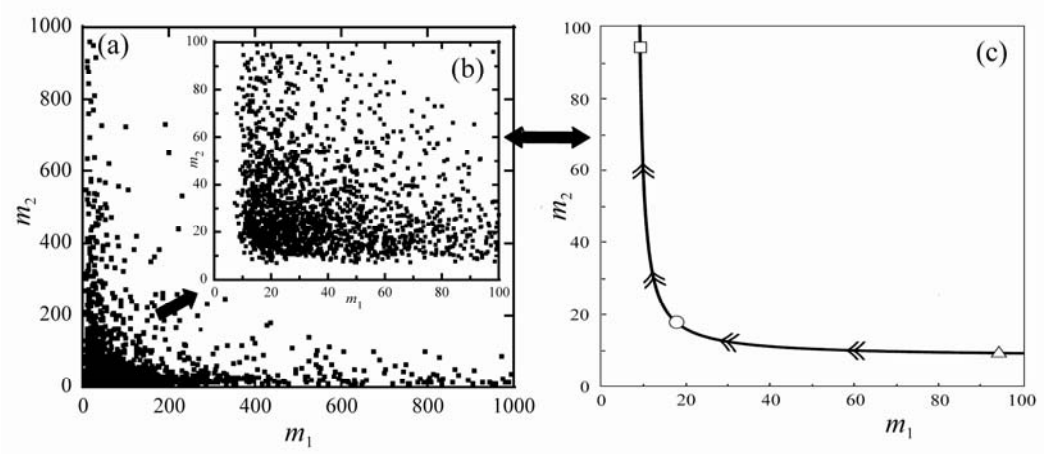

Fig. 2-11 (a) show the simulation results of the relationship between m_1 and m_2 when i = 1, (b) is the enlarged part of (a) when both of m_1 and m_2 are limited within 100 and (c) is analytical results the relationship between m_1 and m_2 quoted from *Ref*. [2-4].

shown in Fig. 2-12 (a) and only exists in a small area. The elastic strain is the biggest around the initial dislocation loop. As time evolves, the elastic strain energy increases and is distributed over the entire simulation region. The values of the elastic strain energy shown in Fig. 2-12 represent the local elastic strain energy in a packet. By integrating the local values over the entire computational domain, the maximum value of the elastic strain energy should be equal to the value of the elastic strain energy when the martensitic transformation finished as shown in Fig. 2-6.

Fig. 2-13 shows the growth process of the lath martensite in 3-D space. The cubic skeleton represents the prior austenite lattice. The martensite phase grows bigger around the initial lath martensite nucleus and becomes full martensite at t^* = 20, which occupies the whole austenite cubic as shown in Fig. 2-13 (d).

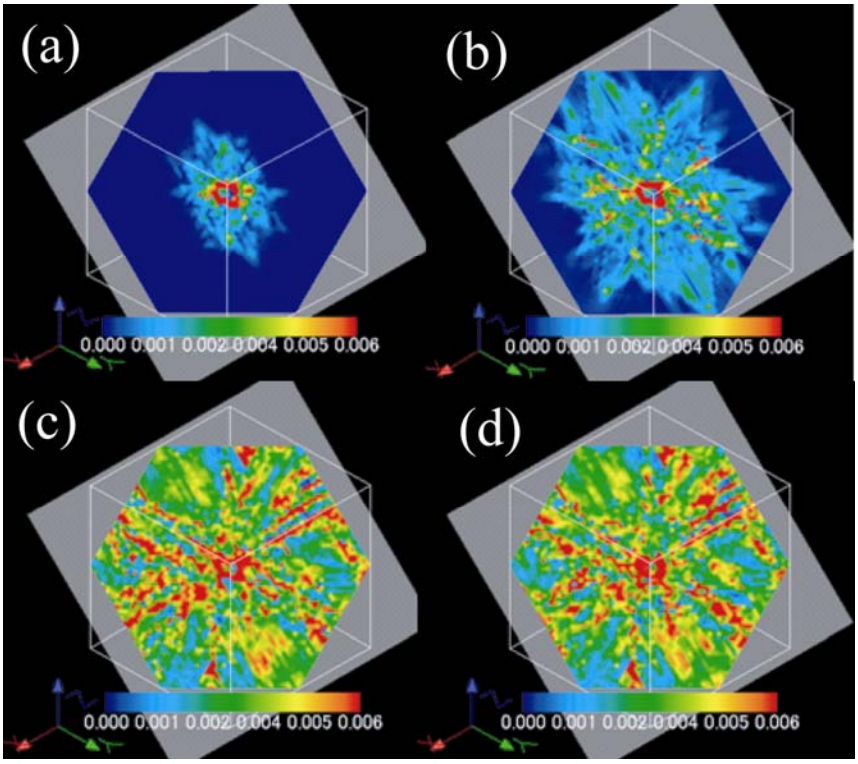

Fig. 2-12 Time evolution of elastic strain energy on {111} plane for (a) t^* = 2, (b) t^* =4, (c) t^* = 8, and (d) t^* = 20 simulated by phase-field model.

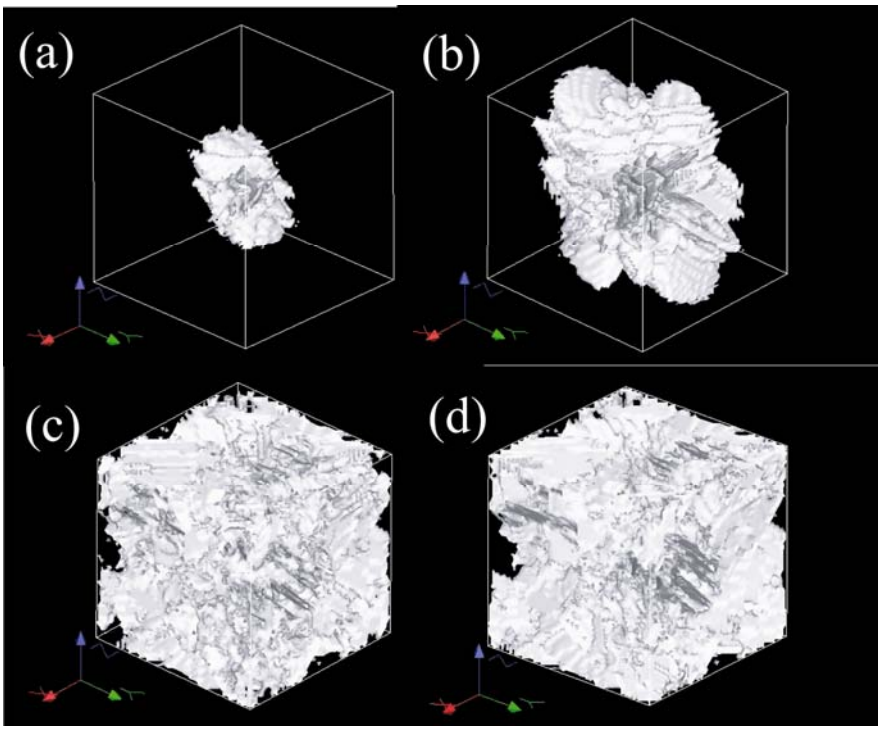

Fig. 2-13 The growth process of lath martensite at (a) t^* = 2, (b) t^* = 4, (c) t^* = 8, and (d) t^* = 20 in 3-D space simulated by phase-field model.

Fig. 2-14 exhibits the time evolution of lath martensite in 3-D space seen from the outside of austenite cubic. The blue cubic represents the austenite phase lattice. The six coloured areas on the surface of the cubic are the six lath variants. At t^* = 2 and 4, the lath martensite only exists inside of the auxtenite cubic as shown in Figs. 2-13 (a) and (b), resulting in that the lath martensite can not be seen from the outside. Therefore, the austenite cubic is still blue as shown in Figs. 2-14 (a) and (b). With the progression of the martensitic transition, the lath martensite phase reaches the surface of the austenite cubic and can be seen from the outside of the austenite cubic as shown in Fig. 2-14 (c). When the martensitic transformation is completed, the lath martensite phase spreads all over the surface of austenite cubic as shown in Fig. 2-14 (d).

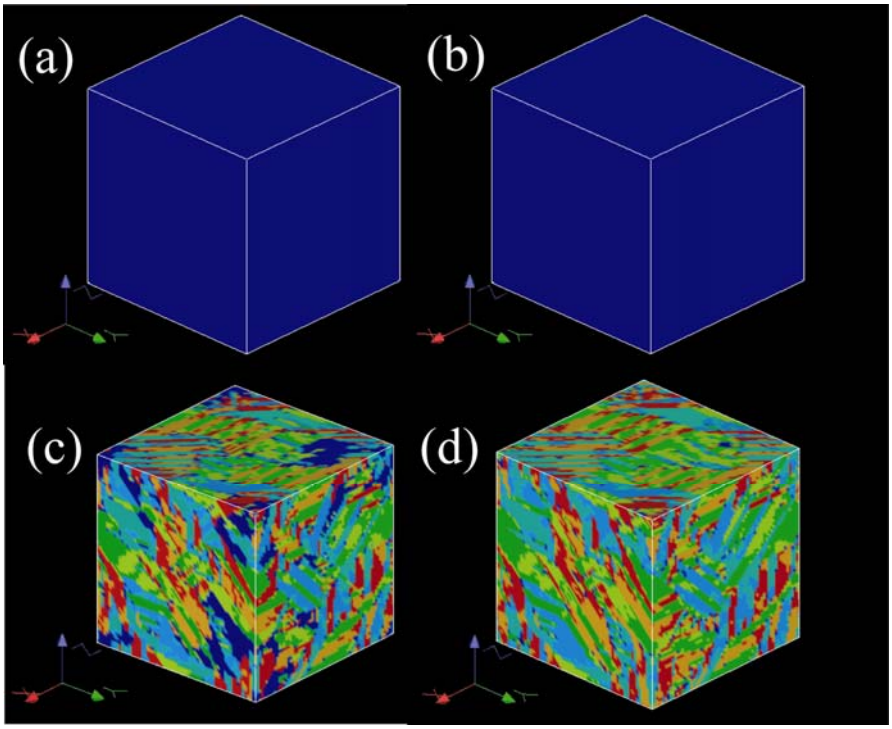

Fig. 2-14 Time evolution of lath martensite at (a) t^* = 2, (b) t^* = 4, (c) t^* = 8, and (d) t^* = 20 in 3-D space observed from the outside of austenite cubic simulated by phase-field model. Each color represents a lath variant.

2.5 Conclusions

On the basis of the two types of slip deformation (TTSD) model for the formation of lath martensite, an elasto-plastic phase-field model was constructed. Furthermore, the morphological evolution of lath martensite in Fe-0.1C mass% steel was simulated by the elasto-plastic phase-field model in 3-D space. It was observed that the full martensite phase can be obtained by releasing the large elastic strain caused by the Bain deformation, via the two types of independent dislocation slips. Moreover, origin of the morphology of lath martensite such as sub-blocks, as seen in commercial steels, can be understood. The relationship of plastic deformation between the two slip systems simulated by phase-field model is consistent with the analytical calculation using by TTSD model. This indicates the validity of the TTSD model for the formation of lath martensite phase. It was proved that the phase-field model was a promising tool to predict the dynamic microstructural evolution of lath martensite.

References

2-1. A. Shibata, S. Morito, T. Furuhara, T. Maki, Scripta Mater. 53 (2005) 597-602.

2-2. S. Morito, X. Huang, T. Furuhara, T. Maki, N. Hansen, Acta Mater. 54 (2006) 5323-5331.

2-3. A. Shibata, Acta Mater. 57 (2009) 483-492.

2-4. K. Iwashita, Y. Murata, Y. Tsukada, T. Koyama, Philos. Mag. 91 (2011) 4495-4513.

2-5. T. Takaki, T. Hasebe, Y. Tomita, J. Cryst. Growth 287 (2006) 495-499.

2-6. A. Yamanaka, T. Takaki, Y. Tomita, Mater. Trans. JIM 47 (2006) 2725-2731.

2-7. A. Yamanaka, T. Takaki, Y. Tomita, Mater. Sci. Eng. A 480 (2008) 244-252.

2-8. R. Kobayashi, Physica D 63 (1993) 410-423.

2-9. J.A. Warren, W.J. Boettinger, Acta Metall. Mater. 43 (1995) 689-703.

2-10. S.R. Shenoy, T. Lookman, A. Saxena, A.R. Bishop, Phys. Rev. B 60 (1999) R12537-R12541.

2-11. M. Bouville, R. Ahluwalia, Phys. Rev. Lett. 97 (2006) 055701.

2-12. Y. Wang, A.G. Khachaturyan, Acta Mater. 45 (1997) 759-773.

2-13. A. Artemev, Y. Jin, A.G. Khachaturyan, Acta Mater. 49 (2001) 1165-1177.

2-14. Y.M. Jin, A. Artemev, A.G. Khachaturyan, Acta Mater. 49 (2001) 2309-2320.

2-15. W. Zhang, Y.M. Jin, A.G. Khachaturyan, Acta Mater. 55 (2007) 565-574.

2-16. A.G. Khachaturyan, *Theory of Structural Transformations in Solids*. New York: John Wiley and Sons Inc; 1983.

2-17. C.M. Wayman, *Introduction to the Crystallography of Martensitic*

Transformations. New York: Macmillian; 1964.

2-18. B.P.J. Sandvik, C.M. Wayman, Metal. Trans. A 14A (1983) 809-822.

2-19. G.V. Kurdjumov, G. Sachs, Zeitschrift fur Physik 64 (1930) 325-343.

2-20. Y.U. Wang, Y.M. Jin, A.M. Cuitino, A.G. Khachaturyan, Acta Mater. 49 (2001) 1847-1857.

2-21. N. Zhou, C. Shen, M. Mills, Y. Wang, Philos. Mag. 90 (2010) 405-436.

2-22. N. Saunders, A.P. Miodownik, *CALPHAD*. Pergamon; 1998.

2-23. J.S. Rowlinson, J. Stat. Phys. 20 (1979) 198.

2-24. J.W. Cahn, J.E. Hilliard, J. Chem. Phys. 28 (1958) 258-267.

2-25. M. Hillert, Acta Metall. 9 (1961) 525.

2-26. Y.U. Wang and A.G. Khachaturyan, Mater. Sci. Eng. A 438-430 (2006) 55-63.

2-27. T. Mura, *Micromechanics of Defects in Solids*, *2nd Rev. ed*. Dordrecht: Kluwer Academic Inc.; 1991.

2-28. J. Kundin, H. Emmerich, J. Zimmer, Philos. Mag. 90 (2010) 1495-1510.

2-29. Japan Institute of Metals ed.*Metals data book*, *third ed*. Tokyo: Maruzen; 1993.

2-30. S. Morito, H. Tanaka, R. Konishi, T. Furuhara, T. Maki, Acta Mater. 51 (2003) 1789-1799.

Chapter 3

Prediction of Maximum Dislocation Density in Lath Martensite by Phase-field Simulation

3.1 Introduction

It is known to us that the martensitic microstructures must be characterized accurately in terms of orientation, morphology, transformation dislocation density, and retained austenite. In recent years, Morito et al. observed the martensitic orientation and microstructures by means of TEM, SEM, and EBSD **[3-1~3-4]**. Spanos et al. adopted EBSD and serial sectioning to establish 3-D morphology of martensite lath **[3-5]**, which provided further detailed insights into lath orientation, distributions, and shapes.

In order to accommodate the large strain induced by martensitic transformation, high dislocation density is inevitable in lath martensite. Wayman classified the dislocations in the martensite phase into two types: transformation dislocations and interface dislocations **[3-6]**. Morito et al. used a TEM method to measure the dislocation densities in both nickel steels and carbon steels, and they reported that the dislocation density for lath martensite is approximately 1.11×10^{15} m^{-2} in a Fe-0.18C steel and 3.8×10^{14} m^{-2} in a Fe-11Ni steel **[3-7]**. In addition, Cong et al. used the X-ray diffraction (XRD) method to evaluate the dislocation density of lath martensite in low carbon steels (0.02–0.09C mass%). The dislocation density is 4.87×10^{14} m^{-2} in a Fe-10Cr-5W-0.02C steel **[3-8]**. As mentioned in Chapter 2 about the TTSD model,

during martensitic transformation, a lot of dislocations contribute to the formation of lath martensite. However, after the phase transition, some dislocations are resided in the martensite crystal, which can be observed by experiments. While some dislocations pass through out of the martensite crystal, which may be used for forming the lath boundaries. This part of dislocations cannot be observed by experimental observation. In this study, we focus on the estimation of the total dislocations for the necessity of the formation of lath martensite, which is wrriten as ρ_{lim}. On the basis of TTSD model, all of the dislocations (ρ_{lim}) contribute to plastic accommodation, the maximum dislocation density can be evaluated from the plastic strain.

In TTSD model **[3-9]**, the plastic deformation is assumed to be realized by dislocation slips along two independent slip systems. In this study, the total dislocations for the necessity of the formation of lath martensite steel is counted by simulation using an elasto-plastic phase-field model based on the TTSD model, and the result is compared with the experimental results reported until date.

3.2 Evaluation method

In TTSD model (Chapter 2), it is assumed that the plastic deformation for martensitic transformation is accommodated thoroughly by the dislocation slips along the two kinds of slip systems $[101](\bar{1}01)_{\alpha'}$ and $[\bar{1}01](101)_{\alpha'}$ as shown in Fig. 3-1 (a) and each slip system can be taken as a combination of two $a/2\langle 111\rangle_{\alpha'}$ dislocation slips with the Burgers vectors of $\mathbf{b_1}$ and $\mathbf{b_2}$ as shown in Fig. 3-1 (b).

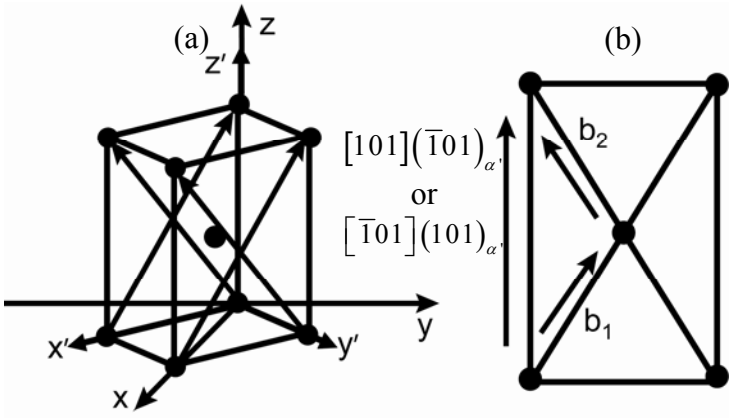

Fig. 3-1 Skeleton of plastic deformations along two slip systems, i.e., $[101](\bar{1}01)_{\alpha'}$ and $[\bar{1}01](101)_{\alpha'}$. $\mathbf{b_1}$ and $\mathbf{b_2}$ are the Burgers vector for the two slip systems.

The idea for using the phase-field method to model a dislocation is established by Nabarro **[3-10]** that dislocations can be taken as a set of coherent misfitting platelet inclusions. For simplisity, a dislocation loop is described as a sheared pletelet with thickness and the region inside the platelet is sheared by a Burgers vector **b [3-11]**. By extending this discription to a spatial region with a population of dislocations, the average plastic strain, p_{ave}, caused by dislocation slip is given by

$$p_{ave} = \frac{|\mathbf{b}|}{D}, \tag{3-1}$$

where $|\mathbf{b}|$ is the magnitude of the Burgers vector and D is the average distance between the neighboring slip planes, that is, dislocation planes. For a real case, the slip planes should arrange randomly as shown in Fig. 3-2 (a). For simplicity, it is assumed that the intervals between neighboring slip planes are the same, as shown in Fig. 3-2 (b), resulting in the reasonability of Eq. (3-1). Seen from Fig. 3-2 (b), if the number of lattice planes between two adjacent slip planes for each slip system is m,

then the value of D can be given by

$$D = m \times d_{hkl} . \tag{3-2}$$

The distance between the $(hkl)_{\alpha'}$ planes is given by

$$d_{hkl} = \frac{1}{\sqrt{\frac{h^2}{a_{\alpha'}^2} + \frac{k^2}{a_{\alpha'}^2} + \frac{l^2}{c_{\alpha'}^2}}}, \tag{3-3}$$

where h, k, and l are the Miller indices of the slip planes, and $a_{\alpha'}$ and $c_{\alpha'}$ are the lattice parameters of the martensite phase.

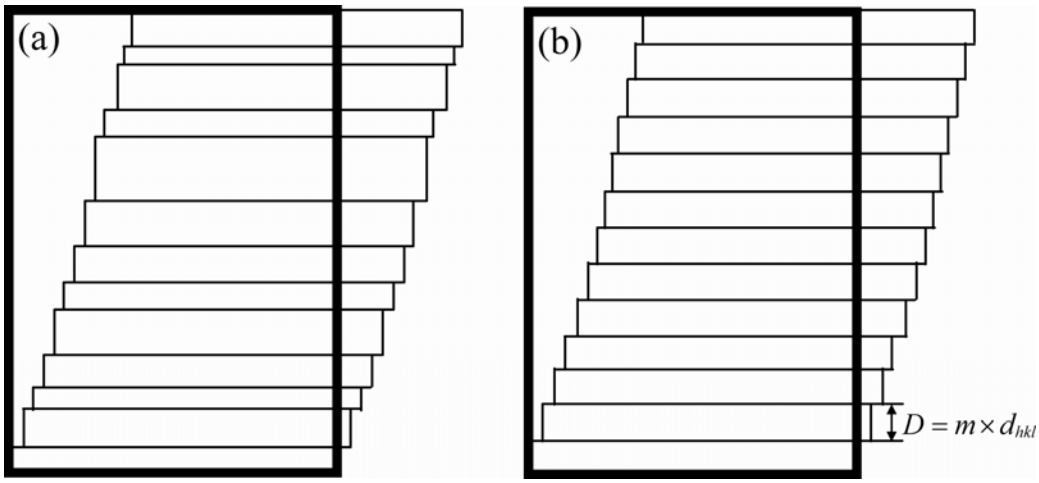

Fig. 3-2 Slip deformation skeleton of the (100) plane along the direction of $[101](\bar{1}01)_{\alpha'}$ or $[\bar{1}01](101)_{\alpha'}$ for (a) a random state and (b) an assumed state.

In the martensitic transformation, ρ_{lim} should contribute to the plastic deformation for moderating the strain by Bain deformation. Here, we give the distance between neighboring dislocations by a rough estimation as

$$D \approx 1/\sqrt{\rho_{\text{lim}}} . \tag{3-4}$$

Eq. (3-4) is given by the original definition of dislocation density, which is equal to the number of dislocations in unit area as shown in Fig. 3-3. It is assunmed that the

dislocations rank with equal intervals not only in the direction of Burgers vector **b**, but also in the direction of slip normal **n**. After such declaration, Eq. (3-4) is reasonable as a rough estimation.

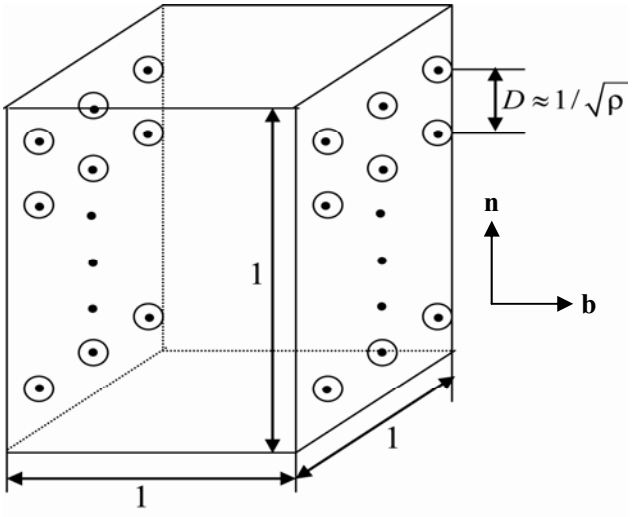

Fig. 3-3 Skeleton of the dislocations in unit volumn and each side of the cube is 1.

Assuming that all of the dislocations contriute to the plastic deformation, the value of D can be estimated from the average plastic strain p_{ave}, which is available from the simulation results by using phase-field model. As mentioned above, TTSD model is based on $[101](\bar{1}01)_{\alpha'}$ and $[\bar{1}01](101)_{\alpha'}$ slip systems in bct crystals. Therefore, the value of D evaluated from Eq. (3-1) is the distance between the neighboring slip planes along $[101](\bar{1}01)_{\alpha'}$ or $[\bar{1}01](101)_{\alpha'}$. To obtain the total dislocations for the necessity of the formation of martensite phase in a real case, the value of D along $\langle 101\rangle_{\alpha'}$ should be transformed to the value along $\langle 111\rangle_{\alpha'}$. By inserting the values of $D_{(101)}$ estimated from Eq. (3-1) and $d_{(101)}$ in Eq. (3-2), we can evaluate the number of lattice planes slipping along the $\langle 101\rangle_{\alpha'}$ system, $m_{(101)}$. As a result, the number of lattice planes slipping actually along the $\langle 111\rangle_{\alpha'}$ direction

$m_{(111)}$ should be twice that of $m_{(101)}$. By substituting the values of $m_{(111)}$ and $d_{(111)}$ into Eq. (3-2), we obtain $D_{(111)}$. Now with the assistance of $D_{(111)}$ and Eq. (3-4), the total amount of dislocations for the necessity of the formation of lath martensite in commercial steels can be evaluated.

3.3 Results and discussion

The phase-field simulation has been described in Chapter 2 and the average value of plastic strain p_{ave}, is obtained from the simulation results by the same model used in Chapter 2. Figure 3-3 shows the simulation result of time evolution of the average value of plastic strain p_{ave}. It averaged all the values of local plastic strain in lath martensite along the two slip systems, $[101](\bar{1}01)_{\alpha'}$ and $[\bar{1}01](101)_{\alpha'}$. The figure indicates that the average plastic strain increases with the progression of martensitic transformation and saturated in 20 time steps at a value of 0.035. This means that the martensitic transformation is accomplished at t^* = 20. Therefore, we use the saturated value of p_{ave} to estimate the maximum dislocation density in a full lath martensite. By inserting the values of p_{ave} and $\left|\mathbf{b}_{(101)\alpha'}\right|$ = 4.06 × 10^{-10} m in pure iron into Eq. (3-1), we calculate the distance between neighboring slip planes $D_{(101)}$ to be 1.16 × 10^{-8} m. Substituting the values of $D_{(101)}$ and $d_{(101)_{\alpha'}}$ = 2.03 × 10^{-10} m into Eq. (3-3), the value of $m_{(101)}$ is estimated to be 57, and thus $m_{(111)}$ should be 114 for the actual slip systems in the martensite phase. By substituting the values of $m_{(111)}$ and $d_{(111)_{\alpha'}}$ = 1.66 × 10^{-10} m into Eq. (3-3) again, we calculated $D_{(111)}$ to be 1.89 × 10^{-8} m. Once the value of $D_{(111)}$ is known, the maximum dislocation density in a practical steel is

evaluated to be 2.8×10^{15} m^{-2} from Eq. (3-2). The simulation result is almost twice of the experimental result in a Fe-0.1C mass% steel (1.55×10^{15} m^{-2}) measured by Kehoe et al. using a TEM method **[3-12]**. The simulation result is definitely higher than the experimental result with respect to the value, but the orders of the dislocation density are the same. As mentioned in 3.2, the maximum dislocation density ρ_{lim} considers the total dislocations for the necessity of the formation of lath martensite. In this sense, the calculation result is natural and right higher than the observed dislocation density.

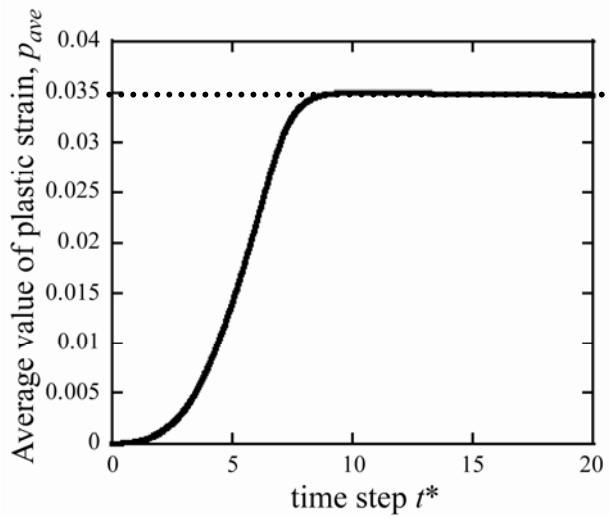

Fig. 3-3 Simulation result of the time evolution of average value of the plastic strain p_{ave}.

In our calculation, only the dislocations in the martensite phase are considered. In fact, the surrounding austenite phase should also contain some dislocations because of the strain originating from the martensite phase and they may be inherited into the lath martensite phase during martensitic transformation **[3-6]**. However, it is argued that if the surrounding austenite phase is deformed during martensitic transformation,

it will help to accommodate part of the strain in the martensite phase, thus resulting in the loss of dislocation density in the martensite phase itself. This loss and the dislocations stored in the surrounding austenite phase cancel each other out. Therefore, the maximum dislocation density in a full martensite should be almost equal to our result. In other words, during martensitic transformation, the total strain containing the surrounding austenite phase is considered to be represented by the dislocations in this study, although the quantitative evaluation should be done in the future.

3.4 Conclusions

The maximum dislocation density of lath martensite in a Fe-0.1C mass% steel was evaluated by phase-field simulation on the basis of TTSD model. The average value of plastic strain was evaluated to be approximately 0.035 for 20 time steps by phase-field simulation. The evaluated maximum dislocation density in lath martensite was 2.8×10^{15} m^{-2}. This result was reasonable to be higher than the observed dislocation density in value but to be the same in order.

References

3-1. S. Morito, X. Huang, T. Furuhara, T. Maki, N. Hansen, Acta Mater. 54 (2006) 5323-5331.

3-2. S. Morito, H. Tanaka, R. Konishi, T. Furuhara, T. Maki, Acta Mater. 51 (2003) 1789-1799.

3-3. S. Morito, I. Kishida, T. Maki, J. Phys. IV France 112 (2003) 453-456.

3-4. S. Morito, H. Saito, T. Ogawa, T. Furuhara, T. Maki, ISIJ Int. 45 (2005) 91-94.

3-5. D. J. Rowenhorst, A. Gupta, C. R. Feng, G. Spanos, Scripta Mater. 55 (2006) 11-16.

3-6. B. P. J. Sandvik, C. M. Wayman, Metall. Trans. A 14 (1983) 809-822.

3-7. S. Morito, J. Nishikawa, T. Maki, ISIJ Int. 43 (2003) 1475-1477.

3-8. Z. Cong, Y. Murata, Mater. Trans. 52 (2011) 2151-2154.

3-9. K. Iwashita, Y. Murata, Y. Tsukada, T. Koyama, Philos. Mag. 91 (2011) 4495-4513.

3-10. F.R.N. Nabarro, Philos. Mag. 42 (1951) 1224-1231.

3-11. N. Zhou, C. Shen, M. Mills, Y. Wang, Philos. Mag. 90 (2010) 405-436.

3-12. M. Kehoe, P. M. Kelly, Scr. Metall. 4 (1970) 473-476.

Chapter 4

Dislocation Density of Lath Martensite in 10Cr–5W Heat-Resistant Steels

4.1 Introduction

High chromium heat–resistant steel has been widely used in power plants because of its excellent creep properties and low thermal expansion coefficients **[4-1~4-4]**. Even though the carbon content of such heat–resistant steel is relatively low (less than 0.1 mass%), the advanced steels containing refractory elements, such as Mo and W, have high strength at elevated tempretures. The high dislocation density introduced into the matrix through martensitic transformation significantly contributes to the high creep strength of such steel. In such steels, lath martensite always appears, which contains a lot of dislocations but no twins. Therefore, researching the dislocation density in the as-quenched state of high–chromium steel is of great importance.

The dislocation density in lath martensite is on the order of 10^{14}–10^{15} m^{-2} **[4-5~4-10]**. Generally, the dislocation density can be measured by transmission electron microscopy (TEM) techniques, X-ray diffraction (XRD) and neutron techniques. These experimental methods complement with each other. However, for martensitic steel, the dislocation density varies from place to place within the grain on a microscopic scale; therefore, in such an inhomogeneous system **[4-11]** the XRD method has the advantages on that it determines a macroscopic average value

compared to TEM method giving a microscopic local value **[4-11, 4-12]**. In this study, we adopted the XRD technique to measure the dislocation density of lath martensitic steel with low–carbon content (0.02 mass% – 0.13 mass%) and clarified the effect of carbon content on the dislocation density in such steels.

4.2 XRD profile analysis

In the present study, modified Williamson–Hall and modified Warren–Averbach plots were employed to determine the dislocation density from the X-ray profiles **[4-13, 4-14]**. The value of the full width at half maximum (FWHM) obtained from peak fitting is substituted into the following modified Williamson–Hall equation **[4-15]**:

$$\Delta K \cong \frac{0.9}{D} + \sqrt{\frac{\pi M^2 b^2}{2}} \rho^{1/2} K \overline{C}^{1/2} + O\left(K^2 \overline{C}\right). \tag{4-1}$$

In the quadratic form it is:

$$\Delta K^2 \cong (\frac{0.9}{D})^2 + \frac{\pi M^2 b^2}{2} \rho K^2 \overline{C} + O\left(K^4 \overline{C}^2\right), \tag{4-2}$$

where $K = 2\sin\theta / \lambda$ and $\Delta K = 2\cos\theta(\Delta\theta) / \lambda$. Here θ , $\Delta\theta$ and λ are the diffraction angle, full width at half-maximum (FWHM) and wavelength of the X-rays, respectively. θ and $\Delta\theta$ can be obtained by fitting the diffraction profiles. In the case of Cu radiation, $\lambda = 0.15405nm$. D, ρ and **b** are the average grain size, dislocation density and magnitude of the Burgers vector, respectively. M is a constant that depends on the effective outer cut-off radius of the dislocations. O denotes the higher–order terms in $K\overline{C}^{1/2}$. Since M can only be obtained from the tails of the

profiles, taking into account the shape of their dacay, the higher-order term can be negligible. Eq. (4-2) can be transformed into a linear function as

$$[(\Delta K)^2 - \alpha] / K^2 \cong \beta \overline{C}_{h00}(1 - qH^2)/2, \tag{4-3}$$

where α = $(0.9/D)^2$ and $\beta = \pi M^2 b^2 \rho/2$. The value of α is determined to maintain a linear relationship between the left-hand term and H^2 in Eq. (4.3). H is a constant and for a given (*hkl*) reflection it can be given as

$$H^2 = (h^2k^2 + h^2l^2 + k^2l^2) / \left(h^2 + k^2 + l^2\right)^2. \tag{4-4}$$

q is a constant to be determined experimentally, which tells the characterization of dislocations. $\overline{C}_{h00}$ is the average dislocation contrast factor corresponding to the (*h*00) diffraction and is determined by the crystal elasticity and $\overline{C}_{h00} = 0.285$ in a pure iron was employed in this study **[4-16]**. From the linear relationship shown in Eq. (4-3), the value of q can be obtained from the interception on the horizontal axis.

Within the frame of the kinematical theory of scattering the diffraction profiles are the convolution of the so-called size and distortion profiles, I^S and I^D, respectively: $I^F = I^S \times I^D$, where the superscript *F* indicates physical profile, i.e., free or stripped from instrumental effects. The earliest diffraction experiments and theoretical considerations have shown that size broadening is diffraction-order independent, whereas strain broadening increases with diffraction order. The increase strain part of broadening, however, reveals *hkl* anisotropy. The strain anisotropic broadening is caused by the presence of dislocations and can be rationalized by the dislocation contrast factors *C*, in the modified Williamson-Hall plot. So in this study,

we use the strain broadening to estimate the dislocation density. The Fourier transformation of $I^F = I^S \times I^D$ is written as **[4-15]**

$$A_L = A_L^S A_L^D = A_L^S \exp[-2\pi^2 L^2 \mathbf{g}^2 \left\langle \varepsilon_{\mathbf{g},L}^2 \right\rangle], \tag{4-5}$$

where *S* and *D* indicate size and distortion, respectively, and *L* is the Fourier length. $\left\langle \varepsilon_{\mathbf{g},L}^2 \right\rangle$ is the mean square strain. By taking the logatithm of Eq. (4-5), the basic Warren–Averbach equation can be written as

$$\ln A_L = \ln A_L^S - 2\pi^2 L^2 \mathbf{g}^2 \left\langle \varepsilon_{\mathbf{g}}^2 \right\rangle \quad . \tag{4-6}$$

The mean square strain, which can be evaluated for different kinds of lattice defects, especially for dislocation reads as

$$\left\langle \varepsilon_{\mathbf{g}}^2 \right\rangle = \frac{\rho C \mathbf{b}^2}{4\pi} \ln(\mathrm{Re}/L), \tag{4-7}$$

By inserting Eq. (4-7) in Eq. (4-6), the modified Warren–Averbach equationis given by **[4-17]**

$$\ln A(L) \cong \ln A^S(L) - \rho \frac{\pi b^2}{2} L^2 \ln\left(\frac{R_e}{L}\right)\left(K^2 \overline{C}\right) + Q\left(K^4 \overline{C}^2\right). \tag{4-8}$$

Here, *A(L)* is the real part of the Fourier coefficients of the *(hkl)* diffraction peak depending on the *L*. The superscript S in the term ln *A(L)* means that this term is related to the crystal size. The Fourier length *L* is defined as below **[4-18]**

$$L = n a_3, \tag{4-9}$$

where *n* are intergers and a_3 is the unit of the Fourier length in the direction of the diffraction vector **g**. $a_3 = \lambda / 2(\sin\theta_2 - \sin\theta_1)$, where the diffraction profile is measured in the angular range $\theta_1 \sim \theta_2$ and λ is the wavelength of the X-rays. ρ is the dislocation density and **b** is the Burgers vector. R_e is the effective outer cut-off

radius of dislocation. $\bar{C}$ is the average contrast factor of dislocation, which is given by **[4-19]**,

$$\overline{C} = \overline{C}_{h00}\left(1 - qH^2\right) . \tag{4-10}$$

By inserting the value of q obtained from modified Warren–Averbach plot in the equation above, the value of $\overline{C}$ can be known. By inserting the values of *A(L)* and $\overline{C}$ into Eq. (4-8), the plot between ln *A(L)* and $K^2\overline{C}$ is available, which is the modified Warren–Averbach plot. The coefficient of the second term in Eq. (4-8) is taken as a function of *Y*, which is arranged as

$$\frac{Y}{L^2} = \rho\frac{\pi b^2}{2}(\ln R_e - \ln L). \tag{4-11}$$

The value of *Y* can be obtained by fitting the modified Warren–Averbach plot. Then we can get a linear relationship between Y/L^2 and ln *L*. Therefore, the value of ρ is determined from the gradient of the linear relationship in Eq. (4-11).

4.3 Experimental procedures

The 10Cr–5W commercial steels containing 0.02, 0.03, 0.09, and 0.13 mass% C (hereafter 10Cr–5W steels) were prepared by austenization at 1323 K for 1 h, followed by quenching into water to obtain a full martensite microstructure. The chemical compositions of these alloys are listed in Table 4-1. Each steel sample was cut into a proper size and polished mechanically with emery papers down to #2000, followed by buff polishing with Al_2O_3 powders down to 0.3 μm. Furthermore, electropolishing was performed to remove the extra dislocations introduced by mechanical polishing. The electropolishing was carried out using a 10% $HClO_4$ acetic

acid solution at 273K with a voltage of 30V.

Table 4-1 Chemical compositions of 10Cr–5W specimens (mass%).

Steel	C	Cr	V	Nb	W	Co	B	N	Ni	Fe
Fe–Cr–W–0.02C	0.02	10.08	0.06	0.06	5.01	3.00	0.011	0.020	1.55	Bal.
Fe–Cr–W–0.03C	0.03	10.04	0.00	0.00	4.96	2.99	0.011	0.020	1.53	Bal.
Fe–Cr–W–0.09C	0.09	10.06	0.06	0.06	4.96	3.00	0.011	0.019	1.54	Bal.
Fe–Cr–W–0.13C	0.13	10.05	0.06	0.06	4.93	3.00	0.011	0.020	1.54	Bal.

For the XRD analysis, the diffraction profiles of the (110), (200), (211), (220), (310), and (222) reflections were measured using a conventional diffractometer (Rigaku UltimaIV X–ray diffractometer) with Cu $K\alpha_1$ and $K\alpha_2$ radiation operating at 40kV and 40mA with a scan speed of 0.25° min^{-1}.

4.4 Results and discussion

The dislocation density of a series of 10Cr–5W steel samples was measured by XRD method. On the basis of the analytical method mentioned in Chapter 4.2, the XRD analysis were performed. Fig. 4-1 shows the peak deconvolution of the (211) reflection in 10Cr–5W–0.02C steel as a representative result. The clear circles in Fig. 4-1 represent the measured data, which agrees well with the regression lines. In such plots, only the peak obtained from Cu $K_{\alpha1}$ radiation was required. Hence, each peak was separated into $K_{\alpha1}$ radiation and $K_{\alpha2}$ radiation using the Lorentz function and the FWHM value of each peak was estimated from the fitting results.

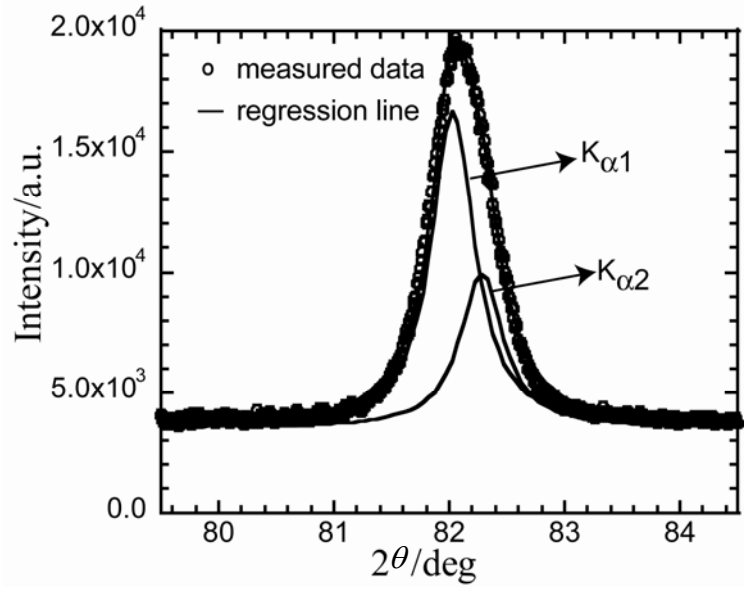

Fig. 4-1 Measured data of the (211) reflection and the fitting profiles using the Lorenz function in 10Cr–5W–0.02C steel.

As the analytical procedures are the same for each sample with different carbon contents, only the analytical procedure for the 0.02 C mass% steel is presented as a representative example. The data obtained from the XRD profiles of 10Cr–5W–0.02C steel is listed in Table 4-2, which shows the diffraction angles, θ and FWHM, $\Delta\theta$ for the six reflections. By inserting these data into Eq. (4-3), $\alpha = 10^{-5}$ nm^{-1} and q = 2.04 were derived from the linear relationship between $(\Delta K^2 - \alpha)/K^2$ and H^2, as shown in Fig. 4-2. The value of α is determined to guarantee the linear relationship shown in Fig. 4-2. Following that, the value of q was substituted into Eq. (4-8) and the modified Warren–Averbach plot was obtained as shown in Fig. 4-3. The range of L is chosen to be from 40 to 90 in order to obtain the full tail part of the profiles shown in Fig. 4-3. The second term on the right hand of Eq. (4-8) was derived by fitting a series of quadratic curves automatically. As a result, $\rho = 4.87 \times 10^{14}$ m^{-2} was determined

from the linear relationship explained in Eq. (4-11), as shown in Fig. 4-4. To be noted that all the solid dots represent the experimental results and lines are regression results shown in Figs. 4-2, 4-3 and 4-4.

Table 4-2 The XRD data of each reflection in 10Cr–5W–0.02C steel.

Bragg reflection	2θ/deg	FWHM/deg
110	44.56	0.113
200	64.85	0.250
211	82.03	0.227
220	98.50	0.344
310	115.76	0.595
222	136.15	0.569

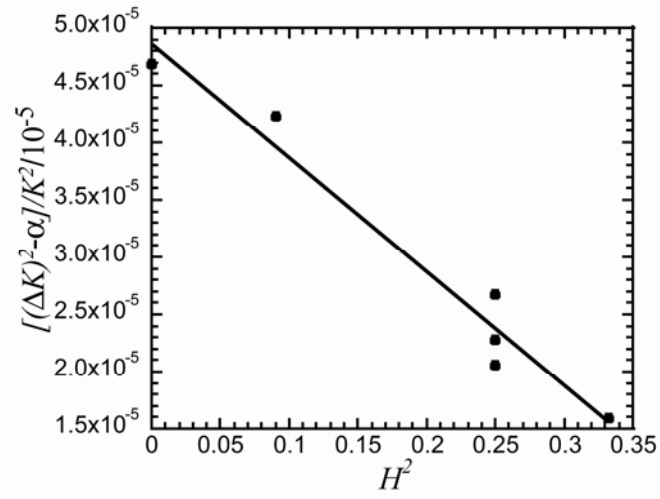

Fig. 4-2 Linear relationship between $(\Delta K^2 - \alpha)/K^2$ and H^2 in Eq. (4-3).

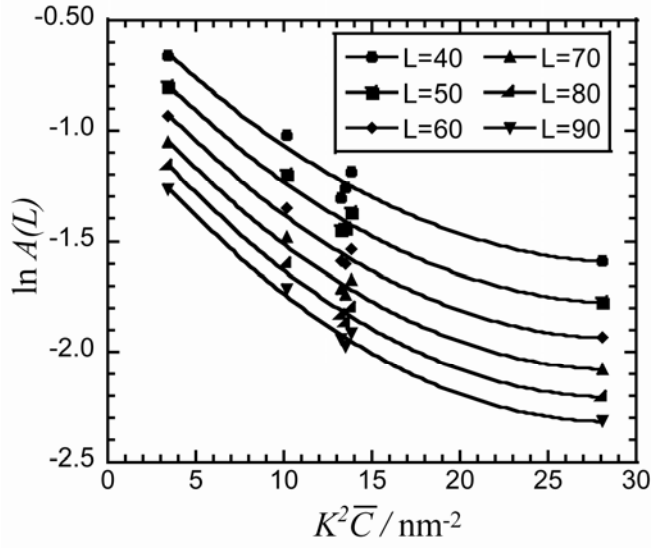

Fig. 4-3 Modified Warren-Averbach plot from Eq. (4-8).

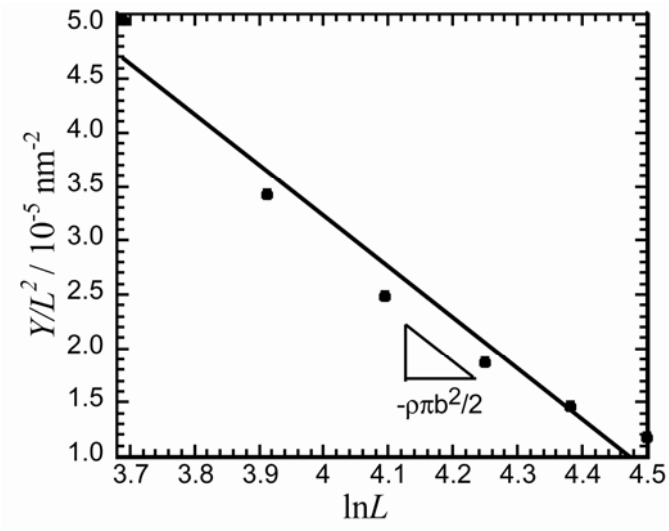

Fig. 4-4 Y/L^2 versus ln L plot according to Eq. (4-11).

The dislocation density in the other three steel samples was derived in a manner similar to that in the 10Cr–5W–0.02C steel sample. For each steel, the dislocation density was measured for three times by selecting the different positions on the surface of the specimen to reduce the measurement deviation. The average dislocation density for each steel sample is shown in Fig. 4-5. Note that the dislocation density

increased slightly with the increase of carbon content. The error bars for each sample are shown within a reasonable range, indicating that the measurments of the three times are authentic. For comparison, the results in Morito's study **[4-20]** are also plotted in the Fig. 4-5. As known to us that the ratio of the lattice parameters in the martensite phase (i. e., c/a) increases with the increase of carbon content, which causes the volume strain for the martensitic transformation to increase, resulting in the increase of dislocation density. In the present study, we focused on detecting the dislocation density in the range of low–carbon range of 0.02–0.13 mass% C, because the dislocation density in such a small range is crucial to the mechanical properties of heat-resistant steels.

The rate of change in dislocation density with the carbon content in our study is considered to be consistent with Morito's data. However, Morito et al. did not detect the dislocation density in such a low–carbon range (less than 0.1mass% C) except in the steel with 0.0026 mass% C (C free) and they determied that the average dislocation density in Fe–0.0026C was 6.5×10^{14} m^{-2}. Interpolating their results suggests that the dislocation density in their study is higher than our results within the low–carbon content range by a factor of ~1.5. One possible reason may be due to the difference in measuring methods. We adopted the XRD method, which gives the average information in bulk materials, compared to the TEM method adopted by Morito, which gives a microscopic local value. Furthermore, it can be said that when the density becomes greater than 10^{14} m^{-2}, it is difficult to accurately measure the dislocation density by means of TEM, because of the complicated image contrasts

from the sample, particularly in the martensite phase with small lattice rotation, containing such a high dislocation density. On the other hand, the existence of W may be one of the possible reasons resulting in the difference between our research and Morito's study. Anyhow, it needs further investigations to verify the effect of W on dislocation density.

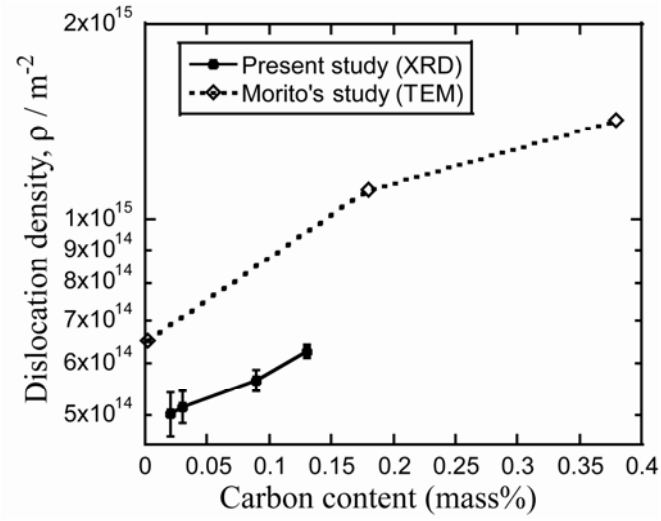

Fig. 4-5 Change in dislocation density with carbon content in low carbon 10Cr–5W steels. The solid squares represent the results measured by XRD in this study and the clear diamonds represent the results in Morito's study measured by TEM.

Fig. 4-6 shows the change in parameter *q* with carbon content of lath martensite phase in 10Cr–5W steel. The parameter *q* depends on the elastic constants of the crystal and determines the character of the prevailing dislocation, i. e., screw, edge or mixed–type dislocation type. The theoretical values of pure edge and screw dislocations in the martensite phase are obtained numerically in various slip systems based on the elastic constants by using Eq. (4-10). The theoretical values of pure edge and screw dislocations, depending on the elastic constants in martensite phase, are estimated to be 1.2 and 2.8, respectively, by using the elastic constants in pure iron

[4-19, 4-21] due to the unavailability of the elastic constants of martensite phase. As shown in Fig. 4-6, the value of q increases slightly from 2.01 to 2.14 as the carbon content increases from 0.02 to 0.13. This indicates that the prevailing dislocation character is mixed type in the lath martensite phase. Also, the dislocation character is determined by the equation below:

$$f^{edge} = \frac{q_{th}^{screw} - q_{\exp}}{q_{th}^{screw} - q_{th}^{edge}} = 1 - f^{screw}, \tag{4-12}$$

where f^{edge} and f^{screw} are the fractions of edge and screw dislocations, respectively. By inserting the theoretical and experimental values of q into Eq. (4-12), the fraction of edge dislocation is approximately 46%, 44%, 37% and 41% in the 10Cr–5W steels with 0.02C, 0.03C, 0.09C and 0.13C mass%, respectively. It seems that the governing dislocation type does not depend on the carbon content. Even though the prevailing dislocation in lath martensite is mixed type, the screw dislocations exist more than the edge dislocations in each lath martensite steel sample.

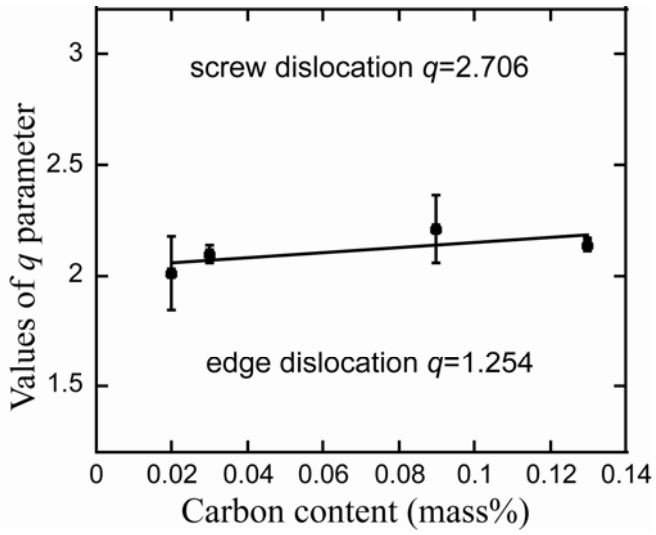

Fig. 4-6 Change in the parameter q with carbon content in low carbon 10Cr–5W steels.

The increase of Vickers hardness shown in Fig. 4-7 indicates that hardness in lath martensite increases not only with the dislocation density but also carbon content. This is consistent with that the high dislocation density is one of the reasons for strenthening the martensite phase with the increase of carbon content.

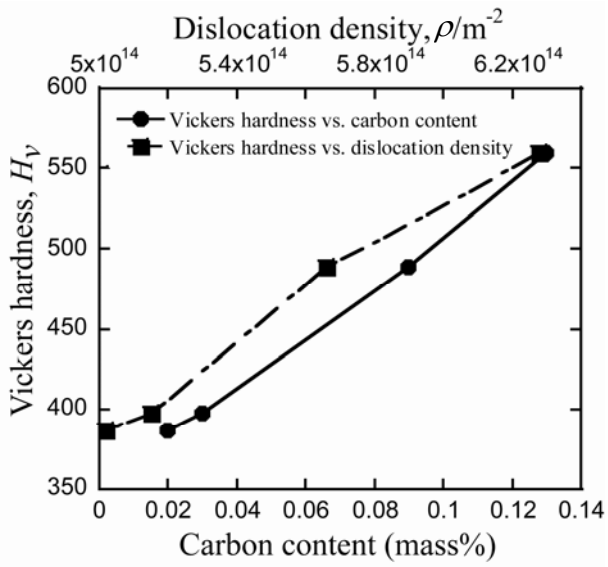

Fig. 4-7 Change in Vickers hardness with carbon content and dislocation density in as-quenched low carbon 10Cr–5W steel.

4.5 Conclusions

The dislocation density in 10Cr–5W steels containing 0.02, 0.03, 0.09 and 0.13C (mass %) was determined to be ~10^{14} by the XRD method. It was found that the dislocation density increased with the increase of carbon content. It is argued that the increases of the carbon content results in the increase of lattice parameters in the martensite phase (i. e., c/a). This change causes the increase of volume strain for the martensitic transformation, resulting in the increase of dislocation density. Although, the dislocation densities in present study are lower than the previous reports, the slope

of the linear relationship between dislocation density and carbon content in our study is consistent with Morito's study. The prevailing dislocation character is mixed type in the lath martensitic steels with different carbon content, although the screw dislocations exist more than edge dislocations in each steel. Moreover, the hardness in lath martensite steel was also detected. It is found that the hardness increases not only with the increase of carbon content, but also with the increase of dislocation density. This result rightly verifies that the high dislocation density can enhance the strength in steels.

References

4-1. F. Masuyama, Tetsu-to-Hagane 80 (1994) 587-592.

4-2. S. Straub, P. Polcik, W. Besigk, W.Blum, H. Konig, K. H. Mayer, Steel Res. 66 (1995) 402.

4-3. K. Sawada, M. Takeda, K. Maruyama, R. Ishii, M.Yamada, Y. Nagae, R. Komine, Mater. Sci. Eng. A 267 (1999) 19-25.

4-4. K. Kimura, H. Kushima, F. Abe, Key Eng. Mater.171-174 (2000) 483-490.

4-5. G.R. Speich, Trans. TMS- AIME. 245 (1969) 2553-2564.

4-6. M. Kehoe, P. M. Kelly, Scr. Metall. 4 (1970) 473-476.

4-7. L.A. Nőrstrom, Scand. J. Metall. 5 (1976) 159-166.

4-8. A. Chanda, M. De, S. Kajiwara, Jpn. J. Appl. Phys. 39 (2000) 539-544.

4-9. D.K. Chaudhuri, P.A. Ravindran, J.J. Wert, J. Appl. Phys. 43 (1972) 778-788.

4-10. K. Wakasa, C.M. Wayman, Acta Metall. 29 (1981) 973-990.

4-11. J. Pěsička, R. Kužel, A. Dronhofer, G. Eggeler, Acta Mater. 51 (2003) 4847-4862.

4-12. D. Breuer, P. Klimanek, U. Müle, U. Martin, Z. Metallkd. 88 (1997) 680-686.

4-13. T. Ungár, J. Gubicza, G. Ribárik, A. Borbély, J. Appl. Cryst. 34 (2001) 298-310.

4-14. T. Shintani, Y. Murata: Acta Mater. 59 (2011) 4314-4322.

4-15. T. Ungár, G. Tichy, Phys. Stat. Sol. (a) 171 (1999) 425-434.

4-16. F. Yin, T. Hanamura, O. Umezawa, K. Nagai, Mater. Sci. Eng. A 345 (2003) 31.

4-17. T. Ungár, A. Borbély, Appl. Phys. Lett. 69 (1996) 3173-3175.

4-18. T. Kunieda, M. Nakai, Y. Murata, T. Koyama, M. Morinaga: ISIJ Int. 45 (2005)

1904-1914.

4-19. T. Ungár, I. Dragomir, A. Revesz, A. Borbély, J. Appl. Cryst. 32 (1999) 992-1002.

4-20. S. Morito, J. Nishikawa, T. Maki, ISIJ. Int. 43 (2003) 1475-1477.

4-21. Japan Institute of Metals ed.*Metals data book*, *third ed*. Tokyo: Maruzen; 1993.

Chapter 5

Morphological Observation of Lath Martensite in Fe-Cr-C Steels

5.1 Introduction

Lath martensite is a characteristic product in as-quenched steels with a low or negligible carbon content, such as plain low-carbon steels, low-carbon and low-alloy steels, maraging steels and interstitial free (IF) steels. The morphology of the lath martensite was investigated extensively by optical microscopy (OM) and transmission electron microscopy (TEM) **[5-1~5-6].** The transformation of a parent austenite grain into lath martensite was characterized as a grain subdivision on different length scales to form the unique hierarchical structure in lath martensite. Firstly, the prior austenite grain breaks down to several packets, which are composed of parallel blocks. Each block is further subdivided by laths, which are narrow units with width in the sub-micrometer range. Since the strength and toughness of martensitic steels are strongly related to packet and block sizes **[5-7]**, the characteristics of those substructures are of great importance.

On the other hand, due to the increasing demands for the highly efficient power plants, the heat resistant ferritic steels have become more popular because of its lower thermal expansion coefficient and the higher resistance to thermal fatigue compared to the austenite steels. Recently, some kinds of heat resistant steels have been developed for the structural applications in the power plants **[5-8, 5-9]**. In such steels, there is a

common trend in their alloy compositions, where the carbon content decreases as well as the contents of chromium increases. Such a compositional modification of the steels could improve high tempreture creep strength and lath martensite phase always appears in such steels. The present investigation involves the morphology observation of the typical lath martensite in Fe-9Cr-(0.1, 0.2, 0.4) C mass% steels by OM and EBSD techniques.

5.2 Experimental procedures

A ternary Fe–9Cr–C steel containing 0.1, 0.2, and 0.4C (mass%) were prepared by austenization at 1373 K for 1h, followed by quenching into water and liquid nitrogen for 45 min to obtain a full martensite microstructure. Then they were tempered at 1043 K for 1 h. Their chemical compositions are listed in Table 5-1. The tempered steel samples were cut to a proper size and polished mechanically with emery papers down to #2000, followed by buff polishing with Al_2O_3 powders down to 0.3 μm. After mechanical polishing, the specimens were etched by 5% HCI and picric acid solution for 8s and then the microstructures were observed by OM. For the EBSP observation, each specimen with different carbon content was etched with a 5% picric acid solution followed by the cross section polishing with a JEOL SM–09010 machine. Finally, the crystal orientaion maps of lath martensite in Fe-Cr-C steels were obtained by the EBSP measurement. Kikuchi patterns obtained by the convergent beam method were analyzed by software for orientation determination.

Table 5-1 Chemical compositions of Fe-Cr-C specimens (mass%).

Steel	C	P	S	Cr	Al	N	O	Fe
Fe-Cr-0.1C	0.10	<0.003	0.0012	9.56	0.008	0.0014	0.0035	Bal.
Fe-Cr-0.2C	0.21	<0.003	0.0016	9.00	<0.005	0.0012	0.0018	Bal.
Fe-Cr-0.4C	0.39	<0.003	0.0016	8.94	<0.005	0.0013	0.0013	Bal.

5.3 Results and discussion

5.3.1 OM observation

Fig. 5-1 shows the optical micrographs (OM) of lath martensite in Fe-Cr-C alloys with different carbon contents. In the 0.1C alloy (Fig. 5-1 (a)), large parallel blocks are seen in a packet with strong contrast. The 0.2C alloy, as shown in Fig. 5-1 (b), also exhibits clear block structures, although they are slightly finer than the blocks in the 0.1 C alloy. In the 0.4C alloy (Fig. 5-1 (c)), blocks and packets are finer than those in the lower carbon alloys. In some areas, it is difficult to recognize blocks and packets in the optical micrograph. The substructures of lath martensite tangled with each other. These results are consistent with the results obtained by Morito's study **[5-6]**. The specific packet or block of lath martensite cannot only be determined from the rough OM observation, whereas the microstructure refinement with the increase of carbon content was verified by the visual observation.

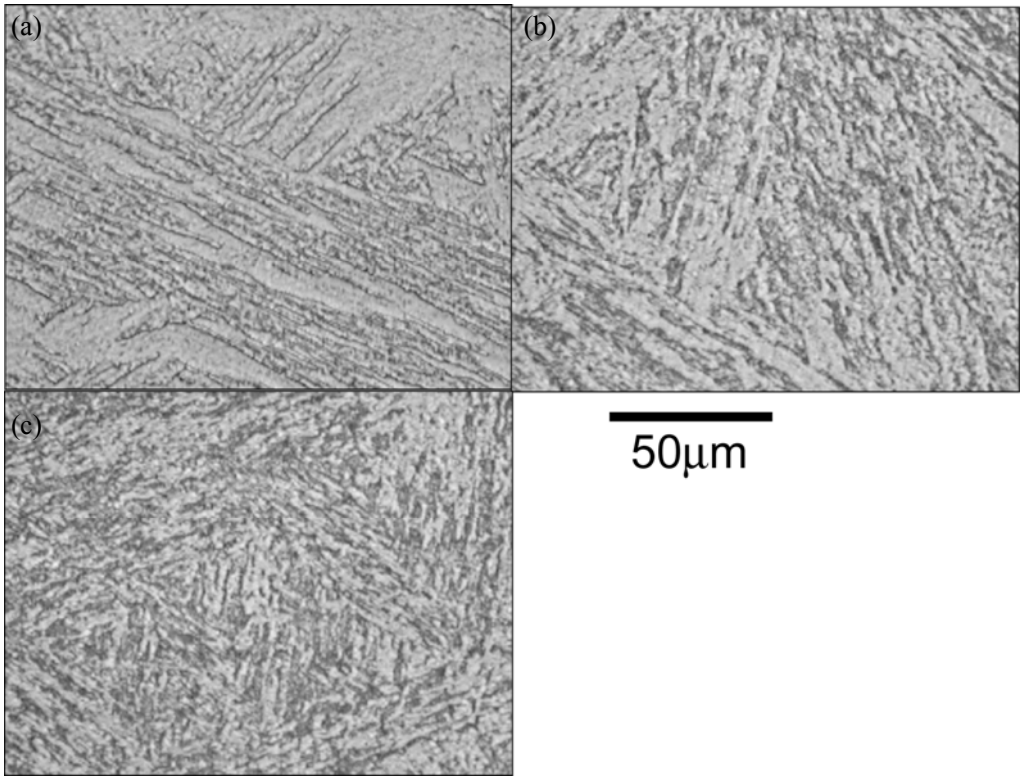

Fig. 5-1 Optical micrographs of lath martensite in a Fe-Cr-0.1C, (b) Fe-Cr-0.2C and (c) Fe-Cr-0.4C alloys.

5.3.2 EBSP observation

Fig. 5-2 shows the crystal-orientation maps obtained by EBSP measurement in the Fe-Cr-C alloys with different carbon content. Generally, the EBSP maps are used to analyze the crystallography of the lath martensite. However, in the present study, we did not focus on the crystallography to distinguish the specific packet or block of lath martensite, but observed the morphology of the lath martensite to analyze the block size of lath martensite. The colored EBSP maps are processed to black-white maps to detect the blocks, where black represents the block boundaries and white represents the blocks. By inputting such maps into the Cos-Mos software, the average

widths of the blocks of lath martensite in the Fe-Cr-C alloys were estimated automatically. In a similar manner, the block sizes of lath martensite in the alloys with different carbon content were obtained. The coloured maps in Fig. 5-2 (a) show the orientaion of laths in Fe-Cr-0.1C alloy. The long and narrow areas with different colour are taken as different blocks of lath martensite and each block contains sub-blocks with similar color contrast. Fig. 5-2 (b) shows the EBSP measurement in the Fe-Cr-0.2C alloy. The block width seems narrower than that in the Fe-Cr-0.1C alloy. But the different blocks with different orientations and each block containing sub-blocks in the same way as the Fe-Cr-0.1C were revealed by Fig. 5-2 (b). Fig. 5-2 (c) shows the crystal-orientation map in Fe-Cr-0.4C alloy. Blocks are finer and more degenerate in comparision with those of the lath martensite in Fe-Cr-0.2C alloy shown in Fig. 5-2 (b). However, the presence of sub-blocks is still recognizable within a block. The EBSP maps also reveal that the microstructure of lath martensite becomes finer with the increase of carbon content, which corresponds to the OM observations.

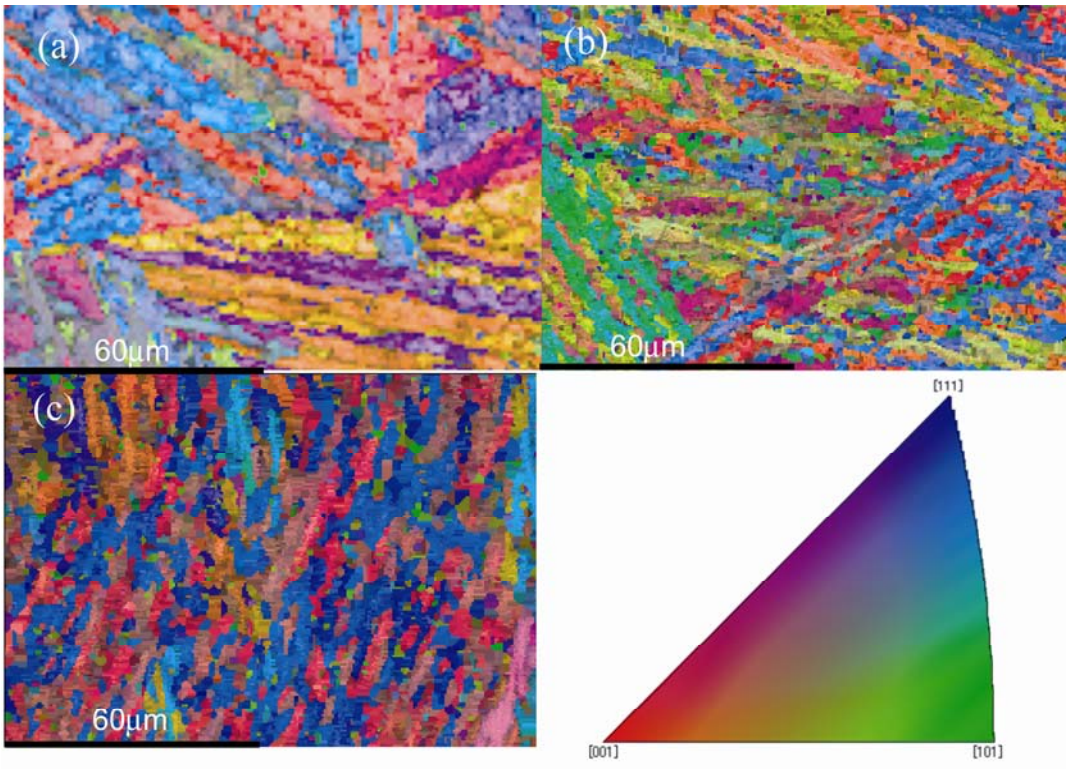

Fig. 5-2 The crystal-orientation map measured by EBSP of (a) Fe-Cr-0.1C (b) Fe-Cr-0.2C and (c) Fe-Cr-0.4C alloys.

Moreover, the EBSP maps are processed to realize the binarization, so that the black and white maps can be obtained as the inputting files for Cos-Mos softwarwe. Fig. 5-3 shows the black and white in Fe-Cr-0.2C steel as an example. Each narrow area shown in Fig. 5-3 is taken as a block of lath martensite phase. By inputting such files into the Cos-Mos siftware, each separated area is taken as a grain, i.e. the block of lath martensite, and the average block size was obtained automatically by counting all the blocks appearing in Fig. 5-3.

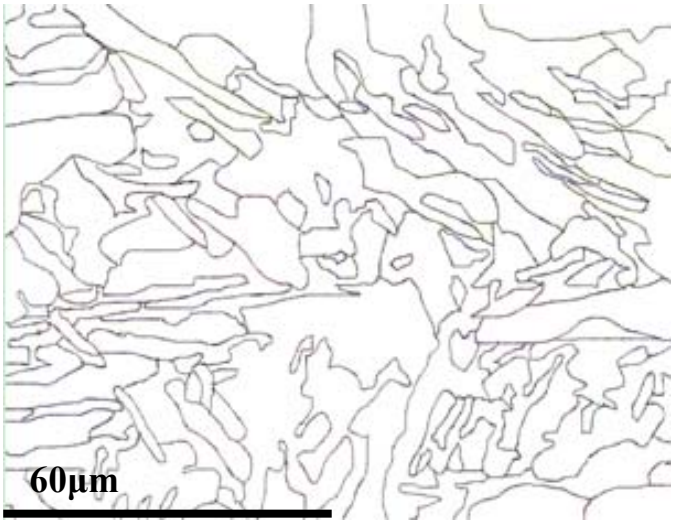

Fig. 5-3 The black-white map of the block boundaries in Fe- Cr-0.2C alloy.

It is to be noted that the so-called block is a long and narrow area, which has width and length. In the present calculation, the each block area is converted to a circle and the radius of the circle is taken as the average block size. Considering the anisotropy of the crystal, for each alloy, three EBSP maps in the directions of ND, TD and RD are used to obtain the average block size as shown in Fig. 5.4. In this way, the block sizes in the alloys with 0.1C, 0.2C and 0.4C were estimated to be 11.39μm, 5.92 μm and 4.30 μm, respectively. And the relationship between the block size and carbon content is plotted in Fig. 5-5.

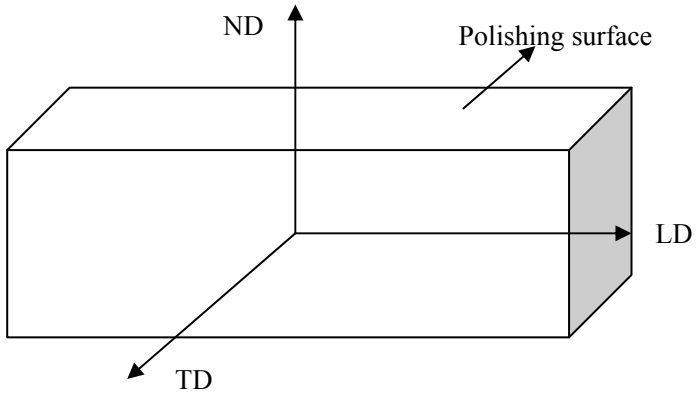

Fig. 5-4 The skeleton of the polished specimens used for EBSP measurement.

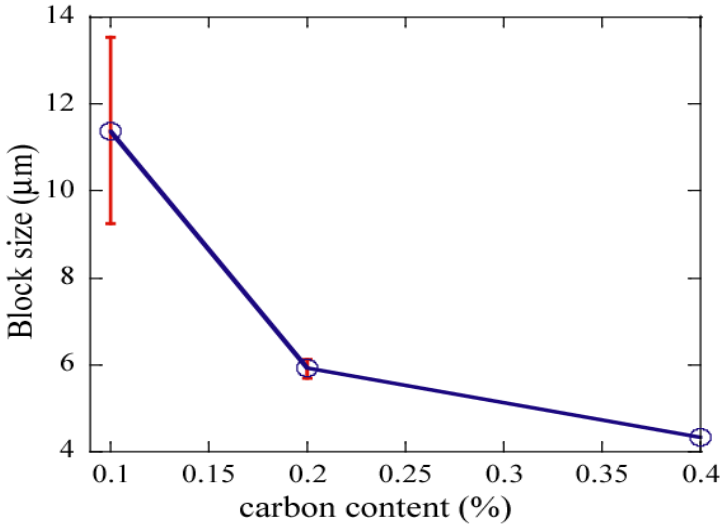

Fig. 5-5 The relationship between the block size and carbon content.

5.4 Conclusions

The morphology and crystallography of lath martensite in Fe-Cr-C alloys with different carbon contents such as 0.1, 0.2 and 0.4 mass% were detected by means of OM and EBSP techniques. The phenomena that the microstructure of lath martensite becomes finer with the increase of carbon content is confirmed both from the OM observations and EBSP measurements. The block sizes of lath martensite in the alloys with 0.1C, 0.2C and 0.4C are evaluated to be 11.39μm, 5.92 μm and 4.30 μm, respectively.

References

5-1. P.M. Kelly, J. Nutting, Proc. R. Soc. Lond. A, 259 (1960) 45-58.

5-2. J.M. Chilton, C.J. Barton, G.R. Speich, J. Iron Steel Inst. 208 (1970) 184.

5-3. G. Krauss, A.R. Marder, Metall. Trans. 2 (1971) 2343-2357.

5-4. T. Maki, K. Tsuzaki, I. Tamura, Trans. ISIJ 20 (1980) 207.

5-5. P.M. Kelly, A. Jostsons, R.G. Blake, Acta Metall. Mater. 38 (1990) 1075-1081.

5-6. S. Morito, H. Tanaka, R. Konishi, T. Furuhara, T. Maki, Acta Mater. 51 (2003) 1789-1799.

5-7. G. Krauss, Metall. Mater. Trans. A, 32 (2001) 861-877.

5-8. T. Fujita, ISIJ Int. 32 (1978) 175-181.

5-9. T. Fujita, Materials and engineering in turbines and compressors, in: R.D. Conroy, et al. (Eds.), Proceedings of the third International CharlesParsons Turbine Conference, The institute of Materials, London, 1995, 493-516.

Chapter 6

General Conclusions

This study aims to investigate the microstructure evolution in lath martensitic steels not only by the experimental tools but also by simulation model. For this purpose, high dislocation density and the hierarchical structure of lath martensite phase are studied in heat-resistant steels by carrying on a series of experiments. On the other hand, an elasto-plastic phase-field model is developed based on the two types of slip deformation (TTSD) model to predict the evolution of martensitic transformation. Moreover, the maximum dislocation density for the necessity of the formation of lath martensite phase in Fe-0.1C (mass %) steel is estimated from the simulation result. Finally, by comparing the experimental results with simulation results, it is found that they are well consistent with each other. The results obtained in each chapter are summarized as follows.

In Chapter 2, the two types of slip deformation (TTSD) model was elaborated in details. By this model, the formation of the lath martensite phase is realized by the Bain deformation followed by plastic deformation along two independent slip systems without any adjustable parameters. In order to prove the validity of the TTSD model, the phase-field method was introduced to simulate the formation of lath martensite in Fe-0.1C mass% steel based on the TTSD model. The blocks and sub-blocks evolution of lath martensite were presented by the simulation. Moreover, it is found that the slip deformation along the two kinds of slip systems occur complementary with each other

in the lath martensite phase. It was found that the relationship of the degree of slip deformation between the two slip systems was well consistent with the analytical calculation by the TTSD model. The morphology of the growing process of lath martensite in 3-D space was also obtained by the simulation. All these results proved the validity of the TTSD model on explaining the formation of lath martensite and the usefulness of the phase-filed model as a powerful tool to predict the microstucture evolution in lath martensite phase.

In Chapter 3, the maximum dislocation density of lath martensite in Fe-0.1C (mass%) steel was estimated from the average plastic strain obtained from the simulation results based on the TTSD model. The evaluated maximum dislocation density was $2.8 \times 10^{15}\,m^{-2}$. This result was reasonable to be higher than the observed experimental dislocation density in value but to be the same in order. Therefore, the TTSD model is considered to be a reliable model to predict the dislocation density in lath martensite.

In Chapter 4, the dislocation density in 10Cr–5W steels containing 0.02, 0.03, 0.09 and 0.13C (mass %) was determined to be $\sim 10^{14}$ by the XRD method. It was found that the dislocation density increased with the carbon content in lath martensitic steels. Even though our results are lower than the previous reports, the slope of the linear relationship between the dislocation density and carbon content in our study in consistent with the previous study. The prevailing dislocation character was mixed type in the lath martensitic steels with different carbon content, and the screw dislocations existed more than edge dislocations in each steel.

In Chapter 5, the microstruture of lath martensite in Fe-Cr-C alloys with different carbon contents such as 0.1, 0.2 and 0.4 mass% were detected by means of OM and EBSP techniques. It was found that the microstructure of lath martensite became finer with the increase of carbon content, which was consistent with the previous reports. On the other hand, the morphology and crystallography of lath martensite were observed from the coloured EBSP maps. Moreover, the block sizes of lath martensite in the alloys with different carbon content were estimated by image analysis. The analytic results also verified that the block sizes decreased with the increase of carbon content.

Generally, the present study for the first time developed an elasto-plastic phase-field model based on the TTSD model to simulate the formation of lath martensite in 3-D space. This is helpful to understand the formation mechanism of lath martensite. At the same, the simulation results prove the validity of the TTSD model on explaining the formation mechanism of lath martensite and the power of phase-field model for microstructure prediction in materials.

Paper List Related to the Present Study

1. “Dislocation density of lath martensite in 10Cr-5W heat-resistant steels”

(Zhenhua Cong and Yoshinori Murata)

Materials Transactions, Vol.52, No. 12 (2011) pp. 2151-2154. (related to Chapter 4)

2. “Phase-field Simulation of the Sub-block Microstructure in Lath Martensitic Steels”

(Zhenhua Cong, Yoshinori Murata, Yuhki Tsukada, Toshiyuki Koyama)

Materials Transactions, in press (related to Chapter 2)

3. “Prediction of the Maximum Dislocation Density in Lath Martensitic steel by Elasto-plastic Phase-field Method”

(Zhenhua Cong, Yoshinori Murata, Yuhki Tsukada and Toshiyuki Koyama)

Materials Transactions, in press (related to Chapter 3)

4. “Elasto-Plastic Phase-Field Simulation of Martensitic Transformation in Lath Martensite Steels”

(Zhenhua Cong, Yoshinori Murata, Yuhki Tsukada, Toshiyuki Koyama)

Philosophical Magazine, submitted (related to Chapter 2)

Acknowledgements

I came to the department of Material Science and Engineering in Nagoya University with little knowledge on the experiments in our major (XRD, EBSD, and so on). Prof. Yoshinori Murata carried me through that hard initial time and let me start my first days of research in Nagoya University. Most importantly, as the adviser, he has always cared my life and supported me in the last year for my Ph. D study, with great tolerance to allow me make mistakes and to instruct me. My sincere thanks should go to him firstly.

Next, I would like to express my appreciation to my country and the Chinese Scholarship Council (CSC) to give me this chance to study in Japan and generous support during the past four years. Prof. Masahiro Morinaga, who interviewed me and gave me the offer to study in the present laboratory, also gives me a deep expression not only on his excellent academic achievements but also on his kindness to China and Chinese people. Dr. Yuhki Tsukada, who served me as the tutor for the first year in Japan, brought my sight out of computer simulations. He lets me think computer simulations in a broad background of both experiments and theories. I received many creative suggestions from Dr. Tsukada. His insight in phase-field simualtion helped me a lot. I will also give my sincere appreciation to Prof. Toshiyuki Koyama in Nagoya Institute of Technology for his useful suggestions and discussions on phase-field simulation. I will always keep a good memory of the days with my group members, from whom, especially Mr. Iwashita and Mr. Fukaya, I learned a lot of things. Also, I would like to appreciate Associate Prof. Yoshihiro Terada and Assistant

Prof. Hiroshi Yukawa for their valuable help and advice on my study. In particular, I am indebted to Mr. Yasutoshi Sasaki and secretary Mrs. Shoko Sanma for their kindly help and chatting in daily life.

This is probably the first time that I put into words to express my appreciation to my parents. They gave me the life, they told me I can do well since the day I left home, and they supported me during my toughest days. My dear boy friend, Dr. Niu Jian never missed a chance to stand by me in front of real troubles and always encourged me when I almostly can not persist in. Finally, I would like to thank all of my friends, who accomponied and helped me during the past four years.

Nagoya, July 2012

Zhenhua Cong